Monthly Notices of the ROYAL ASTRONOMICAL SOCIETY

MNRAS **533,** 2980–2996 (2024) https://doi.org/10.1093/mnras/stae1986
Advance Access publication 2024 August 20

Rossby wave instability and substructure formation in 3D non-ideal MHD wind-launching discs

Chun-Yen Hsu (徐峻彦) [1]★ Zhi-Yun Li,[1] Yisheng Tu (涂以晟) [1] Xiao Hu (胡晓) [1,2] and Min-Kai Lin (林明楷) [3,4]

[1]*Department of Astronomy, University of Virginia, Charlottesville, VA 22904, USA*
[2]*Department of Astronomy, University of Florida, Gainesville, FL 32608, USA*
[3]*Institute of Astronomy and Astrophysics, Academia Sinica, Taipei 10617, Taiwan*
[4]*Physics Division, National Center for Theoretical Sciences, Taipei 10617, Taiwan*

Accepted 2024 August 11. Received 2024 August 6; in original form 2024 July 11

ABSTRACT

Rings and gaps are routinely observed in the dust continuum emission of protoplanetary discs (PPDs). How they form and evolve remains debated. Previous studies have demonstrated the possibility of spontaneous gas rings and gaps formation in wind-launching discs. Here, we show that such gas substructures are unstable to the Rossby wave instability (RWI) through numerical simulations. Specifically, shorter wavelength azimuthal modes develop earlier, and longer wavelength ones dominate later, forming elongated (arc-like) anticyclonic vortices in the rings and (strongly magnetized) cyclonic vortices in the gaps that persist until the end of the simulation. Highly elongated vortices with aspect ratios of 10 or more are found to decay with time in our non-ideal magnetohydrodynamic (MHD) simulation, in contrast with the hydro case. This difference could be caused by magnetically induced motions, particularly strong meridional circulations with large values of the azimuthal component of the vorticity, which may be incompatible with the columnar structure preferred by vortices. The cyclonic and anticyclonic RWI vortices saturate at moderate levels, modifying but not destroying the rings and gaps in the radial gas distribution of the disc. In particular, they do not shut-off the poloidal magnetic flux accumulation in low-density regions and the characteristic meridional flow patterns that are crucial to the ring and gap formation in wind-launching discs. Nevertheless, the RWI and their associated vortices open up the possibility of producing non-axisymmetric dust features observed in a small fraction of PPDs through non-ideal MHD, although detailed dust treatment is needed to explore this possibility.

Key words: accretion, accretion discs – instabilities – MHD – protoplanetary discs.

1 INTRODUCTION

The detection of substructures is a watershed event in protoplanetary disc research (PPDs, e.g. ALMA Partnership et al. 2015; Andrews et al. 2018). While axisymmetric rings, gaps, and cavities are the most common features, non-axisymmetric structures such as spiral arms, lobes, and arcs are also observed. A particular type of non-axisymmetric feature is vortices, which are detected in, for example, HD 142527 using CO emission lines (Boehler et al. 2021) and possibly through near-infrared scattered light (Marr & Dong 2022). Several mechanisms are proposed to produce the substructures, including planet–disc interactions (e.g. Dong, Zhu & Whitney 2015; Bae, Zhu & Hartmann 2017), sintering of volatile ices outside snow lines (Okuzumi et al. 2016), sharp change of disc properties at the dead zone boundary (e.g. Flock et al. 2015; Ruge et al. 2016), secular gravitational instability (e.g. Takahashi & Inutsuka 2016; Tominaga, Takahashi & Inutsuka 2020), zonal flows arising in magnetorotational instability (MRI) turbulence (e.g. Johansen, Youdin & Klahr 2009; Krapp et al. 2018), and non-ideal magnetohydrodynamic (MHD) effects and magnetic disc winds (e.g. Suriano et al. 2017; Riols & Lesur 2019; Cui & Bai 2021).

Magnetic fields have been observed in dense star-forming cores of molecular clouds that collapse to form stars and circumstellar discs (e.g. Galametz et al. 2018; Maury et al. 2018; Le Gouellec et al. 2020). The magnetic field is widely believed to drive the disc evolution, particularly through a magnetized disc wind (e.g. Bai & Stone 2013; Lesur et al. 2022), which removes angular momentum through a laminar torque. Two-dimensional (2D) non-ideal MHD numerical simulations have shown that axisymmetric discs may evolve into stable rings and gaps in wind-launching discs (e.g. Suriano et al. 2017, 2018). More recent 2D non-ideal MHD simulations included detailed chemistry networks in computing the non-ideal MHD coefficients, finding that stable rings and gaps still form robustly, as long as the dimensionless Elsasser number Λ (which measures the degree of field-neutral coupling) is of order unity or larger (e.g. Nolan et al. 2023). The question that naturally arises is: are such axisymmetric rings and gaps stable in three dimensions (3D), particularly to the Rossby wave instability (RWI, Lovelace et al. 1999; Li et al. 2000)?

The RWI occurs when the local Rossby wave is trapped in the non-self-gravitating discs. It may allow non-axisymmetric perturbations

★ E-mail: kdj8qp@virginia.edu

© 2024 The Author(s).
Published by Oxford University Press on behalf of Royal Astronomical Society. This is an Open Access article distributed under the terms of the Creative Commons Attribution License (https://creativecommons.org/licenses/by/4.0/), which permits unrestricted reuse, distribution, and reproduction in any medium, provided the original work is properly cited.

Downloaded from https://academic.oup.com/mnras/article/533/3/2980/7737683 by guest on 19 June 2025

to grow into well-defined vortices (e.g. Zaqarashvili et al. 2021). The RWI has been investigated in the 2D (vertically integrated) linear theories (e.g. Lovelace et al. 1999; Li et al. 2000; Umurhan 2010; Ono et al. 2016) and numerical simulations (e.g. Li et al. 2001; Varnière & Tagger 2006; Lyra et al. 2008; Ono et al. 2018; Cimerman & Rafikov 2023). In the 3D disc (where the vertical structure is accounted for), the RWI has also been studied using both linear theories (e.g. Lin 2012, 2013) and numerical simulations (e.g. Lyra & Mac Low 2012; Richard, Barge & Le Dizès 2013), mostly with a prescribed initially axisymmetric substructure that is observationally motivated but not formed self-consistently. RWI has also been studied in magnetized discs, with toroidal magnetic fields (e.g. Yu & Li 2009), large-scale poloidal magnetic fields (e.g. Yu & Lai 2013), and non-ideal MHD effects (e.g. Cui et al. 2024). The spontaneous formation of rings and gaps in 2D (axisymmetric) non-ideal MHD simulations (e.g. Suriano et al. 2017, 2018; Nolan et al. 2023) provides a rare opportunity to examine the RWI of axisymmetric structures produced through consistent dynamics using 3D simulations. Just as importantly, such 3D simulations also allow us to investigate the formation of disc substructures and the development of RWI in them simultaneously. In this paper, we seek to determine whether the non-linear development of RWI in the rings and gaps formed in the non-ideal MHD wind-launching discs can lead to the formation of vortices and, if so, how they affect the rings and gaps in the radial gas distribution. Vortices are important to investigate because of their potential for dust trapping (see e.g. a recent review by Bae et al. 2023), which may facilitate planetesimal formation.

This paper is organized as follows. We present our simulation setup in Section 2, including the governing equations. Section 3 describes our chemistry model for computing the abundances of charged species, which are used to determine the non-ideal MHD coefficients. In Section 4, we show results of both 2D and 3D simulations, focusing on RWI and its effects on the disc substructure formation. Our results are briefly discussed and summarized in Section 5.

2 SIMULATION SETUP

We use ATHENA++ (Stone et al. 2020) to solve the non-ideal MHD equations:

$$\frac{\partial \rho}{\partial t} + \nabla \cdot (\rho \boldsymbol{V}) = 0, \tag{1}$$

$$\frac{\partial (\rho \boldsymbol{V})}{\partial t} + \nabla \cdot \left(\rho \boldsymbol{V}\boldsymbol{V} + \mathrm{P}^* - \frac{\boldsymbol{B}\boldsymbol{B}}{4\pi} \right) = -\rho \nabla \Phi, \tag{2}$$

$$\frac{\partial e_d}{\partial t} + \nabla \cdot \left[(e_d + \mathrm{P}^*)\boldsymbol{V} - \frac{\boldsymbol{B}(\boldsymbol{B}\cdot\boldsymbol{V})}{4\pi} + \frac{1}{\mathrm{c}} (\eta_{\mathrm{O}} \boldsymbol{J} + \eta_{\mathrm{AD}} \boldsymbol{J}_\perp) \times \boldsymbol{B} \right] = -\rho (\boldsymbol{V} \cdot \nabla \Phi) - \Lambda_{\mathrm{c}}, \tag{3}$$

and the induction equation

$$\frac{\partial \boldsymbol{B}}{\partial t} = \nabla \times (\boldsymbol{V} \times \boldsymbol{B}) - \frac{4\pi}{c} \nabla \times [\eta_{\mathrm{O}} \boldsymbol{J} + \eta_{\mathrm{AD}} \boldsymbol{J}_\perp], \tag{4}$$

where ρ and $\boldsymbol{V}$ are gas mass density and velocity, $\boldsymbol{B}$ is the magnetic field, $P^* = P + B^2/(8\pi)$ is the total (thermal [P] and magnetic) pressure, $\Phi = -GM/r$ is the gravitational potential of the central star, $e_d = \rho V^2/2 + P/(\gamma - 1) + B^2/(8\pi)$ is the energy density, γ is the adiabatic index, $\boldsymbol{J}$ is the current density, $\boldsymbol{J}_\perp = \boldsymbol{B} \times (\boldsymbol{J} \times \boldsymbol{B})/(B^2)$ is the component of $\boldsymbol{J}$ perpendicular to the magnetic field, η_{O} and η_{AD} are the Ohmic and ambipolar diffusivities, and Λ_{c} is the cooling term.

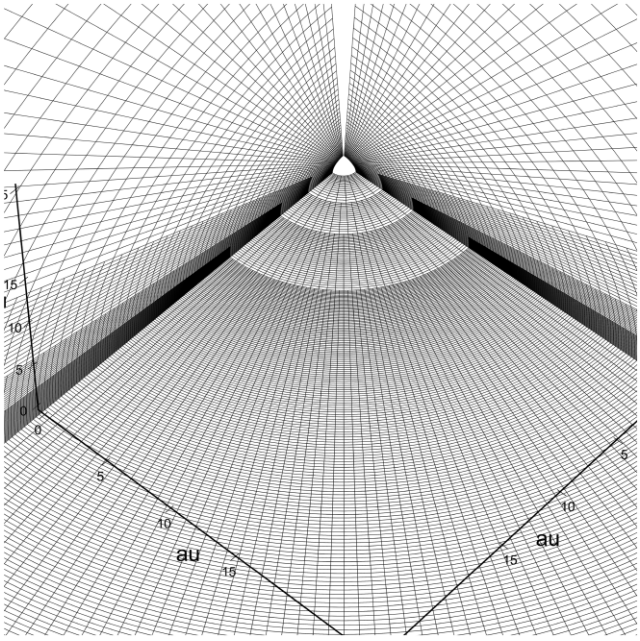

Figure 1. The inner part of the 3D grid, showing three levels of SMR.

2.1 Simulation domain

We use spherical coordinates (r, θ, ϕ) to perform the 2D (axisymmetric, with quantities independent of ϕ) and 3D simulations. The simulation domain goes from 1 to 316 au in the radial direction, 0.05 to $\pi - 0.05$ in the polar direction, and, for 3D simulations, from 0 to 2π in the azimuthal direction. We use a logarithmic grid in the radial direction, with 80 base cells and a ratio of 1.07416 for the sizes of two adjacent cells. The grid is uniform in the polar direction, with 96 cells at the root level. For 3D simulations, we use 32 base cells in the azimuthal direction. Three levels of static mesh refinement (SMR) are used, with the grid size changing by a factor of two between adjacent levels, as indicated in Fig. 1. Specifically, the finest level extends from 10 to 100 au in the radial direction and about 2.5 scale heights (~ 0.13 rad) below to above the mid-plane. The disc scale height is resolved by about 12.6 grids. The second and third finest levels cover, respectively, 5.57 to 176 au and 3.14 to 316 au radially and a polar region within 0.25 and 0.5 rad of the mid-plane.

2.2 Boundary conditions

We use modified outflow boundary conditions at both inner and outer radial boundaries. At the inner boundary, instead of copying gas density and pressure from the innermost active zone to ghost zones, we apply the same power law used in the gas initialization to extend gas density and pressure to ghost zones. For gas velocity, the azimuthal velocity follows a Keplerian curve, and the other two components are copied from the innermost active zone while preventing mass from outside from entering the simulation domain. Reflective conditions are used for the θ boundaries, and periodic boundary conditions are applied in the azimuthal direction.

2.3 Initial conditions

We perform two types of simulations: (i) 2D simulations with an initial hydrostatic equilibrium state and a magnetic field generated from vector potential to ensure a divergence-free B field (i.e. $\nabla \cdot \boldsymbol{B} =$

Downloaded from https://academic.oup.com/mnras/article/533/3/2980/7737683 by guest on 19 June 2025

0) and (ii) 3D simulations that restart from 2D simulations either at relatively late times or near the beginning.

We adopt the initial temperature and density profiles used in Hu et al. (2022). Specifically, we divide the simulation domain into a cold, dense disc and a hot, low-density corona, with a constant aspect ratio, $h/r = 0.05$, where h is the disc scale height. We limit the cold, dense portion to two scale heights above (and below) the mid-plane, that is, in the region $\pi/2 - \theta_0 < \theta < \pi/2 + \theta_0$, where $\theta_0 = \arctan(2h/r)$. The gas density and temperature in the disc mid-plane both follow a power law with index $p = -1.5$ and $q = -1$, respectively:

$$\rho(r, \pi/2) = \rho_0 (r/r_0)^p \qquad (5)$$
$$T(r, \pi/2) = T_0 (r/r_0)^q,$$

where $r_0 = 1$ au is the radius of the inner boundary of the computational domain, and $\rho_0 = 2.667 \times 10^{-10}\,\mathrm{g\,(cm^{-3})^{-1}}$ and $T_0 = 570$ K are the density and temperature at r_0. To ensure a smooth transition between the cold disc and hot corona, we adopt the following vertical profile for the temperature:

$$T(r,\theta) = \begin{cases} T(r,\pi/2) & \text{if } |\theta - \pi/2| < \theta_0 \\ T(r,\pi/2)\,\exp[(|\theta-\pi/2| & \\ \quad -\theta_0)/\theta_0 \times \ln(160)] & \text{if } \theta_0 \le |\theta - \pi/2| \le 2\theta_0 \\ 160\,T(r,\pi/2); & \text{if } |\theta - \pi/2| > 2\theta_0. \end{cases} \qquad (6)$$

We use a quick $\beta_{\rm cool}$ cooling scheme with a cooling time-scale of only 10^{-10} of the local orbital period, so the temperature profile is effectively fixed over time. The vertical density profile is generated based on hydrostatic equilibrium, that is, $v_r = v_\theta = 0$.

The initial magnetic field is computed from the magnetic vector potential used in Zanni et al. (2007):

$$B_r(r,\theta) = \frac{1}{r^2 \sin\theta}\frac{\partial A_\phi}{\partial \theta}, \qquad (7)$$

$$B_\theta(r,\theta) = -\frac{1}{r\,\sin\theta}\frac{\partial A_\phi}{\partial r}, \qquad (8)$$

$$B_\phi = 0, \qquad (9)$$

with

$$A_\phi(r,\theta) = \frac{4}{3} r_0^2 B_{\rm p,0} \left(\frac{r\sin\theta}{r_0}\right)^{\frac{3}{4}} \frac{1}{(1+2\cot^2\theta)^{5/8}}, \qquad (10)$$

where $B_{\rm p,0}$ sets the scale for the poloidal field strength. The magnetic field setup is the same as that of Bai & Stone (2017), Suriano et al. (2018), and Hu et al. (2022). In all our simulations, $B_{\rm p,0}$ is set by plasma $\beta = 10^3$ in the mid-plane.

We perform two types of 3D simulations to investigate (1) whether axisymmetric substructures formed in 2D simulations are stable to RWI and (2) how disc substructures and RWI develop simultaneously. For the first type, we restart in 3D a 2D simulation after it has evolved for a certain amount of time (typically $t_{\rm st} = 2000$ yr) when prominent rings and gaps have formed. For the second type, we restart from the beginning of the simulation ($t_{\rm st} = 0$). Since the focus of the 3D simulations is on RWI, we add a random perturbation to the radial velocity up to 10 per cent of the local sound speed at the time of restart to seed the instability.

3 NON-IDEAL MHD EFFECTS

3.1 Chemical network for charge abundances

To determine the non-ideal MHD coefficients in equation (4), the abundances of charged species must be computed first. We use a reduced chemical network similar to those of Umebayashi & Nakano (1990) and Nishi, Nakano & Umebayashi (1991). Specifically, we include the following elements: H, He, C, O, and Mg. Table A1 in Appendix A lists their initial abundances.

We include cosmic-ray ionization, which dominates the ionization in the bulk of the disc. We adopt a total ionization rate (including ionization of H_2 and He, Umebayashi & Nakano 1990) of $\xi = 10^{-17}\mathrm{s}^{-1}$. The rate equation for species i of the fractional abundance, $x_i \equiv n_i/n_{\rm H}$, can be written as:

$$\frac{1}{n_{\rm H}}\frac{{\rm d}x_i}{{\rm d}t} = \frac{1}{n_{\rm H}}\sum_j k_{\rm cr} x_j + \sum_{j,k} k_{jk} x_j x_k - x_i \sum_m k_{i,m} x_m, \qquad (11)$$

where $k_{\rm cr}$ is the cosmic-ray ionization rate, and k_{jk} and $k_{i,m}$ are the formation and destruction rates by two-body reactions, respectively.

We include three types of reactions in the paper: gas-phase, gas–grain, and grain–grain. Table A2 lists all gas-phase reaction rates used in the paper. The gas-phase reaction rates are adapted from UMIST database (McElroy et al. 2013), with the rate coefficient represented by:

$$k(T) = \alpha_{\rm c} \left(\frac{T}{300{\rm K}}\right)^{\beta_{\rm c}} \exp\left(-\frac{\gamma_{\rm c}}{\rm T}\right), \qquad (12)$$

where $\alpha_{\rm c}$ is the constant factor, $\beta_{\rm c}$ is the power-index of the temperature dependence, and $\gamma_{\rm c}$ measures the energy barrier of the reaction.

We adopt a power law of $n(a) \propto a^{-3.5}$ for the grain size distribution, with the power index of the standard MRN distribution (Mathis, Rumpl & Nordsieck 1977). There are 30 size bins logarithmically distributed from the minimum $a_{\rm min}$ to the maximum $a_{\rm max}$. A grain material density of 3 $\mathrm{g\,(cm^3)^{-1}}$ is adopted. The dust-to-gas mass ratio is set to 0.01. The gas–grain and grain–grain reaction rates are calculated as average reaction rates following Grassi et al. (2019):

$$\langle k_{c,g}(T)\rangle = \frac{\int_{a_{\rm min}}^{a_{\rm max}} \varphi(a) k_{c,g}(a,T){\rm d}a}{\int_{a_{\rm min}}^{a_{\rm max}} \varphi(a){\rm d}a}, \qquad (13)$$

$$\langle k_{g,g}(T)\rangle = \frac{\int_{a_{\rm min}}^{a_{\rm max}}\int_{a_{\rm min}}^{a_{\rm max}} \varphi(a) k_{g,g}(a,a',T)\varphi(a'){\rm d}a{\rm d}a'}{\int_{a_{\rm min}}^{a_{\rm max}}\int_{a_{\rm min}}^{a_{\rm max}} \varphi(a)\varphi(a'){\rm d}a{\rm d}a'}, \qquad (14)$$

where $k_{c,g}(a,T)$ denotes the rate coefficient for gas–grain reactions, and $k_{g,g}(a,a',T)$ is the grain–grain interaction rate coefficient. To simplify the symbol, we note $a_{\rm s} = a_i + a_j$ as the sum of the grain sizes for the grain–grain interaction. We assume a negligible radius for the gas-phase species compared to the grains, so $a_{\rm s} = a_j$ when we calculate $k_{c,g}(a,T)$. Following Nishi et al. (1991) and Grassi et al. (2019), we consider up to two elemental charges sticking on the grains (e.g. $Z = 0, \pm1, \pm2$). Following Draine & Sutin (1987) and Zhao, Caselli & Li (2018), we consider three cases for $k_{c,g}(a,T)$ and $k_{g,g}(a,a',T)$:

$$k^0_{i,j}(a_s,T) = \pi a_s^2 \left(\frac{8k_{\rm B}T}{\pi m_{\rm r}}\right)^{1/2}\left[1 + \left(\frac{\pi e^2}{2a_s k_{\rm B}T}\right)^{1/2}\right] S(T,Z_j), \qquad (15)$$

$$k^-_{i,j}(a_s,T) = \pi a_s^2 \left(\frac{8k_{\rm B}T}{\pi m_{\rm r}}\right)^{1/2}\left(1 - \frac{Z_j}{Z_i}\frac{e^2}{a_s k_{\rm B}T}\right) \cdot\left[1 + \left(\frac{2}{\frac{a_s k_{\rm B}T}{e^2} - 2\frac{Z_j}{Z_i}}\right)^{1/2}\right] S(T,Z_j), \qquad (16)$$

$$k^+_{i,j}(a_s,T) = \pi a_s^2 \left(\frac{8k_{\rm B}T}{\pi m_{\rm r}}\right)^{1/2} \cdot\left[1 + \left(\frac{4a_s k_{\rm B}T}{e^2} + 3\frac{Z_j}{Z_i}\right)^{-1/2}\right]^2 \exp\left(-\frac{\theta_v e^2}{a_s k_{\rm B}T}\right) S(T,Z_j), \qquad (17)$$

where e is the elemental charge, $m_{\rm r} = m_i m_j/(m_i + m_j)$ is the reduced mass, $S(T)$ is the sticking coefficient, and $\theta_v = Z_j^{3/2}/[Z_i(\sqrt{Z_i} + \sqrt{Z_j})]$. $k^0_{i,j}$ is for charged species colliding with

Downloaded from https://academic.oup.com/mnras/article/533/3/2980/7737683 by guest on 19 June 2025

neutral grains (e.g. $Z_i Z_j = 0$). $k^-_{i,j}$ is the rate for opposite charge reactions (e.g. $Z_i Z_j < 0$). $k^+_{i,j}$ is the reaction rate between species with the same electrical properties (e.g. $Z_i Z_j > 0$). If the collisions are between charged species and grains, then the index i and j represent the charged species and grains, respectively. The index i and j represent the lighter and heavier grains for grain–grain interactions. The sticking coefficients $S(T, Z)$ of electrons on grains are taken from Grassi et al. (2019, their table 3). Following Umebayashi & Nakano (1990), we set the sticking coefficients for non-electron charged species on grains to $S(T, Z) = 1$.

3.2 Non-ideal MHD coefficients

Once the charge abundances are known, the ambipolar, Hall, and Ohmic diffusivities can be computed using the standard procedure based on the parallel, Pedersen, and Hall conductivities (e.g. Wardle 2007; Pinto, Galli & Bacciotti 2008):

$$\sigma_{\rm O} = \frac{ec}{B}\Sigma_j n_j |Z_j| \beta_{j,n}, \tag{18}$$

$$\sigma_{\rm H} = -\frac{ec}{B}\Sigma_j \frac{n_j |Z_j| \beta^2_{j,n}}{1+\beta^2_{j,n}}, \tag{19}$$

$$\sigma_{\rm P} = \frac{ec}{B}\Sigma_j \frac{n_j |Z_j| \beta_{j,n}}{1+\beta^2_{j,n}} \tag{20}$$

where

$$\beta_{j,n} = \frac{eZ_j B}{m_j c}\frac{m_j + m_n}{\rho_n R_{j,n}(T)} \tag{21}$$

is the Hall parameter for collisions between the jth charged species and neutral hydrogen, n_j is the number density of the jth species, ρ_n and m_n are the neutral (molecular) hydrogen mass density and mass, respectively, and $R_{j,n}(T)$ is the momentum exchange rate coefficient, which is discussed in detail in Appendix B.

From the conductivities, we can compute the Ohmic, Hall, and ambipolar diffusivities as follows:

$$\eta_{\rm O} = \frac{c^2}{4\pi\sigma_{\rm O}}, \tag{22}$$

$$\eta_{\rm H} = \frac{c^2}{4\pi\sigma_\perp}\frac{\sigma_{\rm H}}{\sigma_\perp}, \tag{23}$$

$$\eta_{\rm AD} = \frac{c^2}{4\pi\sigma_\perp}\frac{\sigma_{\rm P}}{\sigma_\perp} - \eta_{\rm O}, \tag{24}$$

where $\sigma_\perp = \sqrt{\sigma^2_{\rm H} + \sigma^2_{\rm P}}$.

The dimensionless Elsasser numbers for these diffusivities are given by $\Lambda_{\rm O} = \frac{V_{\rm A0}}{\Omega\eta_{\rm O}}$, $\Lambda_{\rm H} = \frac{V_{\rm A0}}{\Omega\eta_{\rm H}}$, and $\Lambda_{\rm AD} = \frac{V_{\rm A0}}{\Omega\eta_{\rm AD}}$, where $V_{\rm A0} = B_0^2/(4\pi\rho_0)$ is the Alfvén speed, with the lower subscript '0' denoting the local quantity at each location, and Ω is the Keplerian angular velocity.

To mimic the better magnetic coupling (and thus reduced diffusivity) due to higher ionization levels expected in the lower density regions near the disc surface and in the disc wind, we follow Suriano et al. (2018) and multiply the magnetic diffusivities in equations (22)–(24) by the following θ dependence:

$$f(\theta) = \begin{cases} \exp\left(-\frac{\cos^2(\theta+\theta_0)}{2(h/r)^2}\right) & \text{if} \quad \theta < \frac{\pi}{2} - \theta_0 \\ 1 & \text{if} \quad \frac{\pi}{2} - \theta_0 \le \theta \le \frac{\pi}{2} + \theta_0 \\ \exp\left(-\frac{\cos^2(\theta-\theta_0)}{2(h/r)^2}\right) & \text{if} \quad \theta > \frac{\pi}{2} + \theta_0 \end{cases}. \tag{25}$$

4 FORMATION OF GAS RINGS AND GAPS IN 2D AND THEIR STABILITY IN 3D

We will mainly consider models with the charge abundances computed from the chemical network discussed in Section 3.1. The abundances are shown in Appendix A (Fig. A1) for an MRN-type grain size distribution from $a_{\rm min} = 0.5$ μm to $a_{\rm max} = 25$ μm. These abundances are saved as a lookup table and referenced during the simulation to compute the non-ideal MHD coefficients in each computational cell. These models are labelled by the letter 'T ' (for 'Table') in Table 1, which lists all 2D and 3D models discussed in the paper. For comparison, we also consider a 2D model with the simple power-law prescription for the dominant molecular ion from Shu (1992) that was used in previous work along a similar line (Suriano et al. 2018; Hu et al. 2022). This model is denoted by the letter 'S' (for 'Shu') in Table 1. The initial Elsasser numbers for these two model types are shown in Fig. A2 of Appendix A for reference.

Table 1. Models.

Name	Description	Starting time $t_{\rm st}$
S-2D	Shu-type power-law ion abundance	0
T-2D	Chemical network	0
T-3D−2000	Chemical network	2000 yr
T-3D−0	Chemical network	0

4.1 2D simulations

We start with a comparison of the 2D (axisymmetric) simulations using the Shu-type power-law prescription (Model S-2D) and the more realistic charge abundances from a lookup table computed from a chemical network including dust grains (Model T-2D). In Fig. 2, we plot a meridional (left panels) and face-on (right panels) view of the simulations at a representative time $t = 2000$ yr when stable rings and gaps are formed. We use cylindrical coordinates (R, ϕ, z) in the meridional plots. The rings and gaps in Model T-2D are more prominent than those in Model S-2D because the gas in the former is better coupled to the magnetic field than in the latter in the bulk of the disc material (see Fig. A2). Our results add weight to the conclusion based on previous work in the literature (e.g. Bai & Stone 2013; Lesur 2021), especially that of Nolan et al. (2023), that ring and gap formation is a robust phenomenon in 2D that is not sensitive to the detailed treatment of the ambipolar diffusivity as long as the disc gas is reasonably well coupled to the magnetic field, with an ambipolar Elsasser number Λ of order unity or larger. The question arises: are the rings (and gaps) formed in 2D stable in 3D, particularly regarding Rayleigh instability and RWI?

One way to check the Rossby wave stability is to compute the quantity $\mathcal{L}(r)$ defined in Lovelace et al. (1999) as a function of radius:

$$\mathcal{L}(r) \equiv \mathcal{F}(r) {\rm S}^{2/\gamma}(r). \tag{26}$$

The result is shown in Fig. 3. Panel (a) shows the radial profiles of the column density of Models S-2D and T-2D at the time shown in Fig. 2. The column density contrast between the rings and gaps in Model T-2D is higher than in Model S-2D, consistent with Fig. 2. Panel (b) of Fig. 3 shows the radial profiles of the quantity $\mathcal{L}(r)$ of Models S-2D and T-2D, where $\mathcal{F}(r) \approx \Sigma/(2\omega_z)$, $\omega_z \equiv \hat{z}\cdot(\nabla\times\boldsymbol{V})$, and ${\rm S} \equiv P/\Sigma^\gamma$ with P denoting the vertically integrated pressure and γ is the adiabatic index. It is formally derived for an adiabatic flow for razor-thin discs, which differs from our case, where strong cooling keeps the flow nearly isothermal locally. In this case, the relevant quantity to evaluate is the inverse of a generalized vortensity, defined as (Lin 2012):

$$\mathcal{H}(r) \equiv \frac{2\Omega\Sigma c_s^2}{\kappa^2} = \frac{\Sigma c_s^2 r}{\partial(r v_\phi)/\partial r} = \frac{\Sigma c_s^2}{\omega_z}, \tag{27}$$

Downloaded from https://academic.oup.com/mnras/article/533/3/2980/7737683 by guest on 19 June 2025

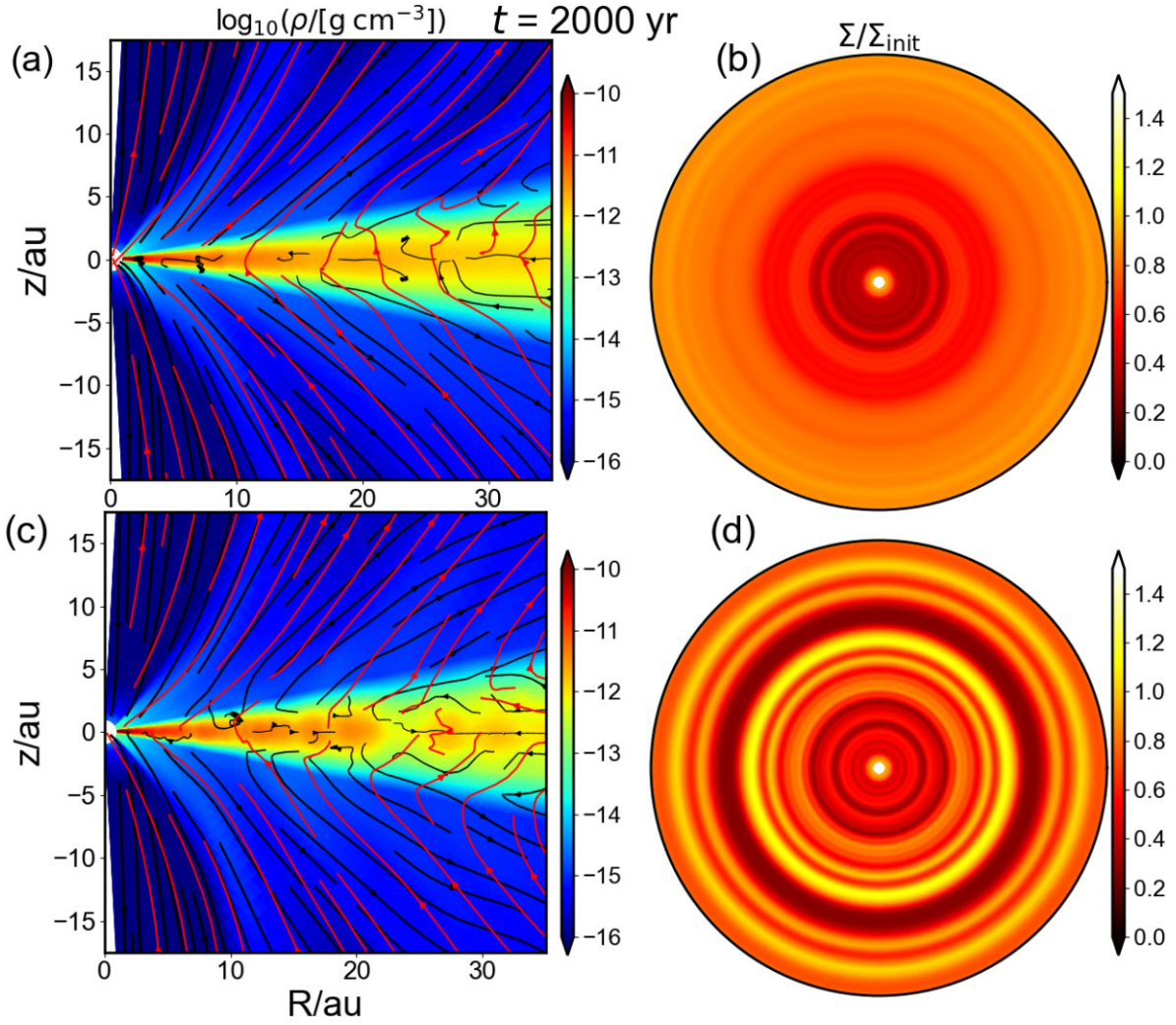

Figure 2. Rings and gaps in 2D Models S-2D (top panels) and T-2D (bottom panels) at a representative time $t = 2000$ yr in the inner disc (up to 35 au in radius). Plotted in panels (a) and (c) are the mass density distribution (colour map), velocity streamlines (black lines with arrows), and magnetic field lines (red lines with arrows) on a meridional plane. A magnetized disc wind is clearly visible in both cases. Panels (b) and (d) display the surface density of the disc normalized to its initial value, highlighting the formation of prominent rings and gaps, especially in Model T-2D.

where κ is the local epicycle frequency. This quantity is plotted in panel (c). In addition, we plot in panel (d) the distribution of the specific angular momentum $r\ v_\phi$ on the disc mid-plane as a function of radius r. A few (limited) regions have specific angular momentum decreasing with radius; they are prone to Rayleigh instability, which may quickly develop to limit the amplitude of the pressure gradient-induced deviation from the background Keplerian rotation in 3D (e.g. Ono et al. 2018).

Lovelace et al. (1999) and Lin (2012) found that a local extremum of $\mathcal{L}(r)$ and $\mathcal{H}(r)$ is a necessary criterion for destabilizing the Rossby waves for adiabatic and locally isothermal flows, respectively. Panels (b) and (c) of Fig. 3 show local extrema are ubiquitous in our case. It indicates that the Rossby waves might grow throughout our simulation domain if there is an initial azimuthal variation to trigger them. However, our simulations do not strictly follow the situation envisioned in Lovelace et al. (1999) or Lin (2012) because of the inclusion of additional physical effects such as the magnetic field, non-ideal MHD effects, and disc winds. In what follows, we will determine whether the rings are indeed unstable to RWI through direct 3D simulations.

4.2 Stability of 2D rings and gaps in 3D

To check the stability of the disc substructures formed in the 2D simulations, we restart Model T-2D (which produced more prominent substructures than the other 2D model, Model S-2D) from the representative time shown in Fig. 2. We include a random perturbation to the radial component of the velocity up to 10 per cent of the local sound speed to seed any potential instability that may grow. The results of the restarted 3D model, T-3D-2000, are shown in Fig. 4. The figure plots the surface density distribution normalized to its initial value at the beginning of the 2D simulation ($t = 0$), the mid-plane mass density normalized to its initial value, the midplane plasma-β_z based on the vertical magnetic field component, and the mid-plane radial velocity normalized by the local sound speed at three representative times: $t = 2340$ (top panels), 2980 (middle), and 3490 yr (bottom panels). The link to an animated version of the figure can be found in its caption.

Fig. 4 and its associated animation clearly show the development of non-axisymmetric structures, which follow the patterns expected for RWI; we will focus primarily on the rings since their azimuthal

Downloaded from https://academic.oup.com/mnras/article/533/3/2980/7737683 by guest on 19 June 2025

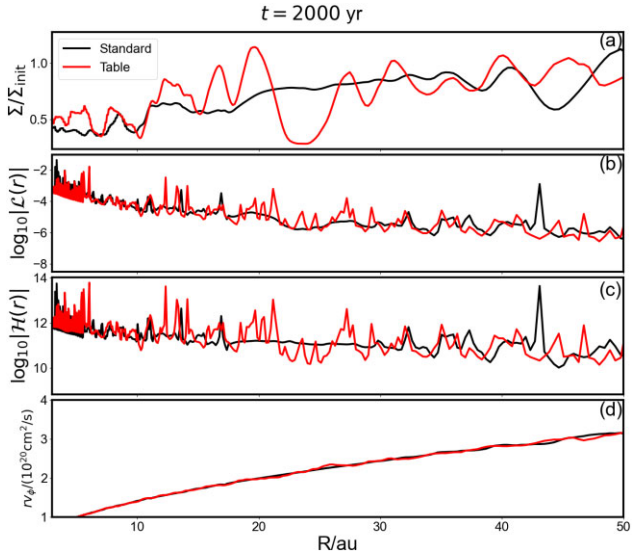

Figure 3. Radial profiles of (a) the surface density of the disc normalized to its initial value, (b) the function $\mathcal{L}(r)$ (defined in equation [26]) that controls the RWI for adiabatic flows, (c) the function $\mathcal{H}(r)$ (defined in equation [27]) that controls the RWI for locally isothermal flows, and (d) the specific angular momentum on the mid-plane, for the discs with rings and gaps shown in Fig. 2. Note the local maximum and the local minimum in the $\mathcal{L}(r)$ and $\mathcal{H}(r)$ profiles in panels (b) and (c) are the positions where the disc may be unstable to the RWI. Regions with specific angular momentum increasing with radius are stable to the Rayleigh instability for rotating flows.

variations show up more clearly in the surface and mass density maps (RWI-induced structures in the gaps will be discussed towards the end of the next subsection). Specifically, the instability first develops in the inner disc and progressively moves to larger radii with longer local dynamical times. For a given ring of roughly constant radius, the azimuthal mode number m of the dominant non-axisymmetric features decreases with time. For example, at the relatively early time of $t = 2340$ yr (or 340 yr after the 3D restart), there are eight well-defined overdense clumps in the midplane mass density distribution that are regularly spaced on the ring at ~ 11 au (panel b), even though the clumps are less visible in the surface density at the same time (panel a). The $m = 8$ mode is even more prominent in the distribution of the mid-plane plasma-β_z, which is much higher inside the overdense clumps than between them (panel c). The same mode also shows up in the midplane radial velocity distribution, with the fastest radial outward motion occurring between the overdense clumps and at a slightly smaller radius (panel d). We note that the time $t = 2340$ yr corresponds to about nine times the local orbital period at the unstable ring location, comparable to the saturation time for the fiducial model studied by Ono et al. (2018).

Similar patterns are observed at the later time $t = 2980$ yr but for a ring at a larger radius of ~ 20 au (compared to ~ 11 au discussed in the last paragraph). Here, the $m = 8$ mode is the most prominent in the radial velocity distribution (panel h), with eight regularly spaced regions of fast inflow at approximately half of the local sound speed. The fast-inflow regions are located slightly outside the visibly perturbed 20 au radius ring, with the inflow apparently displacing the ring inward, producing a regularly spaced undulation in the radial direction, which is also evident in the surface density distribution (panel e). The undulation soon leads to the formation of eight overdense regions similar to those for the inner ring near 11 au at the earlier time $t = 2340$ yr (see panel b), as can be seen from the animated version of the figure (see times around $t = 3000$ yr). There is, therefore, little doubt that the 20 au ring is RWI unstable, with a well-developed $m = 8$ mode at $t = 2980$ yr, corresponding to about 11 local orbital periods, similar to the 11 au ring at a comparable local dynamical time (normalized by the orbital period). The mode is less evident in the mid-plane plasma-β_z distribution because it has more radial substructures than the density distribution, which makes the high plasma-β_z ring near 20 au stand out less than the high mass density ring at a similar radius.

The lack of one-to-one correspondence between the substructures in the plasma-β_z and density distributions is illustrated by the faint ring inside the prominent gap around 10 au, which is barely visible in the density map (panel f) but stands out clearly as a high plasma-β_z ring against the lower plasma-β_z adjacent gaps (panel g). This low-density but high β_z ring is the 11 au ring showing prominent $m = 8$ azimuthal mode at the earlier time $t = 2340$ yr (panel b). At this earlier time, at least seven well-defined rings were located inside the 20 au ring discussed at the later time $t = 2980$ yr, with four outside the prominent 10 au gap and at least three inside. Visible azimuthal structures develop earlier in these (inner) rings than in the 20 au ring, with higher order modes at earlier times. By $t = 2980$ yr, only relatively low-order azimuthal modes (with m of a few) are clearly visible in the density map (panel f). In particular, two prominent arcs (corresponding to the $m = 2$ azimuthal mode) develop in the ring immediately interior to the 10 au ring around $t = 2700$ yr (see the animation of the density map), which has been smeared into a long arc with moderate azimuthal density variation by the time shown in panel (f). The trend for lower order modes to dominate later is consistent with the expected evolution and saturation of RWI modes (see e.g. Ono et al. 2018).

The trend is vividly illustrated by the last frame of the simulation when the surface density and mid-plane density of the 20 au ring become dominated by two well-defined, relatively short, overdense arcs (panels i and j) at $t = 3490$ yr, corresponding to approximately 17 local orbital periods after the 3D restart. By this time, the azimuthal variations of the mid-plane density of the rings at larger radii remain dominated by higher m modes. In particular, an $m = 7$ mode starts to show up clearly in the outermost ring (at ~ 32 au) displayed at the time of panel (j), corresponding to approximately eight local orbital periods, similar to the times (normalized by the local orbit period) when the $m = 8$ mode becomes prominent for the inner 11 au (panel b) and 20 au (panel f) rings.

It is unclear how long the low-order $m = 2$ mode for the 20 au ring at the last frame would survive. A hint for the longer-term evolution of RWI-induced structures comes from the rings at relatively small radii, which evolved for longer local dynamical times than their larger radius counterparts. For example, two prominent overdense (relatively long) arcs develop in the 7.5 au ring around 2650 yr (approximately 31 local orbital periods after the 3D restart), and last until 2760 yr for ~ 110 yr or ~ 5 local orbital periods (see the animated version of the mid-plane density). A single ($m = 1$) overdense arc dominates the appearance of the ring at some of the later times (e.g. $t = 3300$ yr), in agreement with the expectations based on the simpler hydro case (e.g. Ono et al. 2018). However, this is not the case at other times, for example, at the last frame shown in panel (j), where at least two, possibly three, arcs with moderate density enhancements exist. This deviation from the expectations is unsurprising since our simulated disc is more complex than the simplest hydro case (with, e.g. non-ideal MHD and disc wind). In particular, the rings and gaps in our simulation are highly dynamic structures that can gain or lose mass and angular momentum through spatially dependent mass accretion and (magnetized) outflow.

Downloaded from https://academic.oup.com/mnras/article/533/3/2980/7737683 by guest on 19 June 2025

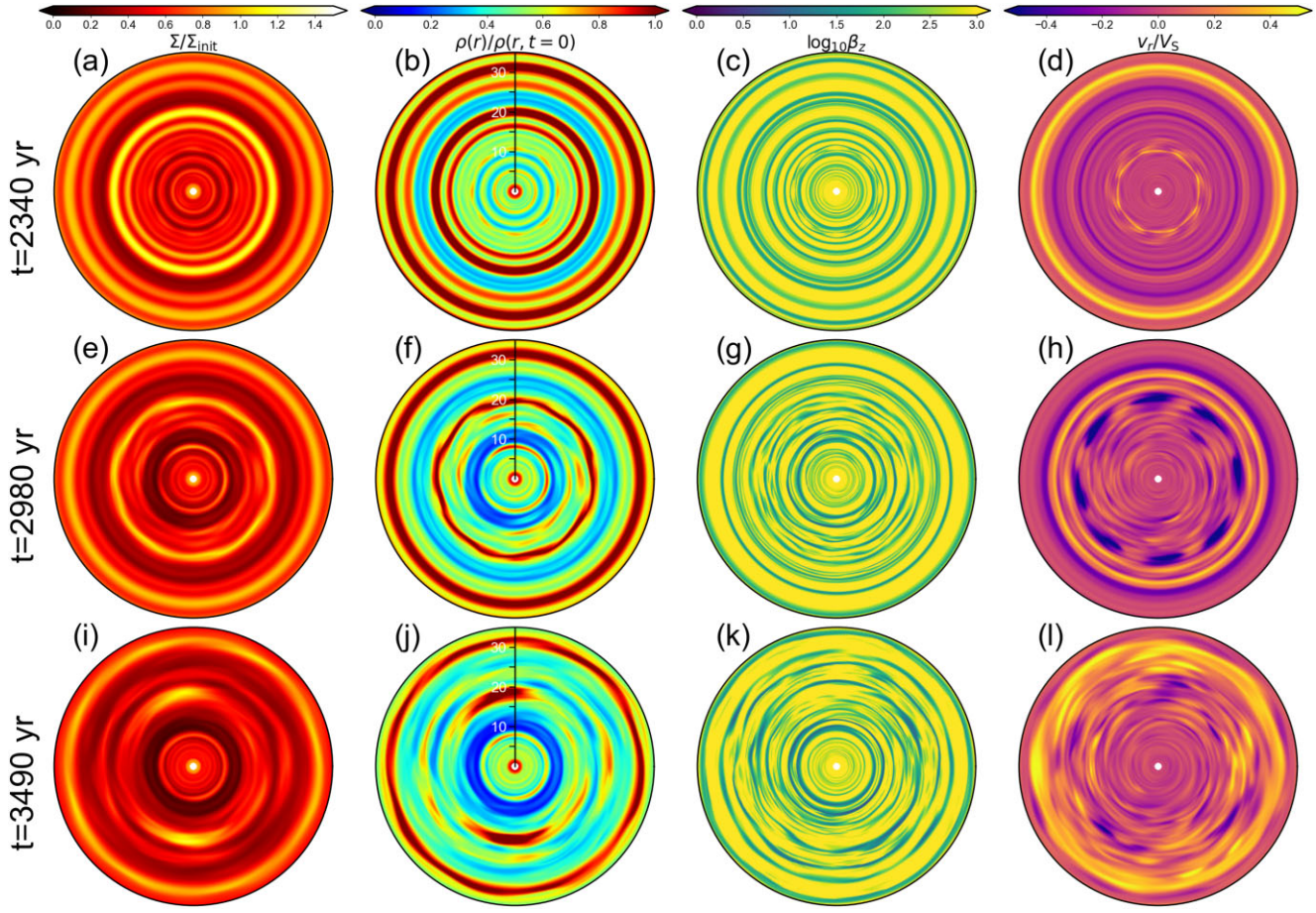

Figure 4. Evolution of 2D rings and gaps in 3D. Plotted in the first column are the surface density distribution normalized to its initial value at three representative times $t = 2340$ (panel a), 2980 (panel e), and 3490 yr (panel i) of Model T-3D-2000 restarted from Model T-2D at $t = 2000$ yr. Similarly, the second, third, and fourth columns show, respectively, the mid-plane mass density normalized to its initial value, the mid-plane plasma-β_z based on the vertical field component B_z alone, and the mid-plane radial velocity normalized by the sound speed. An animated version of the figure can be found on the website: https://virginia.box.com/s/b1wxk512g1xzm371thk9h7w4l1sfl8qk.

To quantify the late-time evolution of different azimuthal modes, we plot in Fig. 5 the mode amplitudes of the azimuthal surface density variations of three representative rings at approximately 5, 8, and 18 au as a function of time normalized by their local orbital period. The low-order $m = 2$ mode (see the red curve) starts to dominate at a time between ~ 15 and ~ 30 local orbital periods; its further evolution is truncated by the termination of the simulation for the 18 au ring (panel a). For the 8 au ring, the $m = 2$ mode decays after ~ 10 local orbital periods and is replaced by the even lower order $m = 1$ mode with a higher peak amplitude (panel b). The $m = 1$ mode decays after ~ 30 orbits. Its longer term evolution is unclear because of the simulation time limit, but a hint is offered by the 5 au ring, which reached ~ 130 orbits. In this case, the $m = 1$ mode is more important than the $m = 2$ mode most of the time after ~ 65 orbits, but the $m = 2$ remains significant and occasionally surpasses the $m = 1$ mode in amplitude. A caveat is that the 5 au ring is on a coarser grid than the other two rings and is resolved azimuthally by only 64 cells (see the statically refined grid in Fig. 1). The relatively low resolution may have affected the growth and saturation of the modes. Nevertheless, it is clear that, as expected for RWI, low-order modes dominate the azimuthal variation of the surface density at late times, with relatively small amplitudes. An implication is that the non-linear development of RWI modifies but does not destroy the rings formed in our non-ideal MHD simulations.

The effects of the RWI modes on rings are further illustrated in panel (j) of Fig. 4, which shows that the 8 au ring remains distinct from its neighbouring gaps (i.e. with a significant axisymmetric $m = 0$ mode) even after a relatively large number (~ 72) of local orbit periods, indicating that non-linear development of RWI modifies rather than destroys the ring. The same is true for rings at smaller radii, such as the one around 5 au, which retains its ring-shaped structure after ~ 133 local orbital periods. To demonstrate the survival of the rings and gaps more clearly, we plot in Fig. 6 the azimuthally averaged surface density distribution of Model T-3D-2000 as a function of radius after its restart at $t = 2000$ yr and compare it to its 2D counterpart Model T-2D. There are some differences between the two models at late times, including a more prominent ring at ~ 5 au in the 2D case and a less empty gap at ~ 10 au in the 3D case. Nevertheless, the azimuthally averaged radial substructures are broadly similar in the two cases, supporting the notion that rings and gaps survive in 3D despite RWI.

4.3 RWI vortex structure

In this subsection, we analyse the structure of the vortices for the 8 au ring at the time $t = 3150$ yr (or 1150 yr after the 3D restart), when

Downloaded from https://academic.oup.com/mnras/article/533/3/2980/7737683 by guest on 19 June 2025

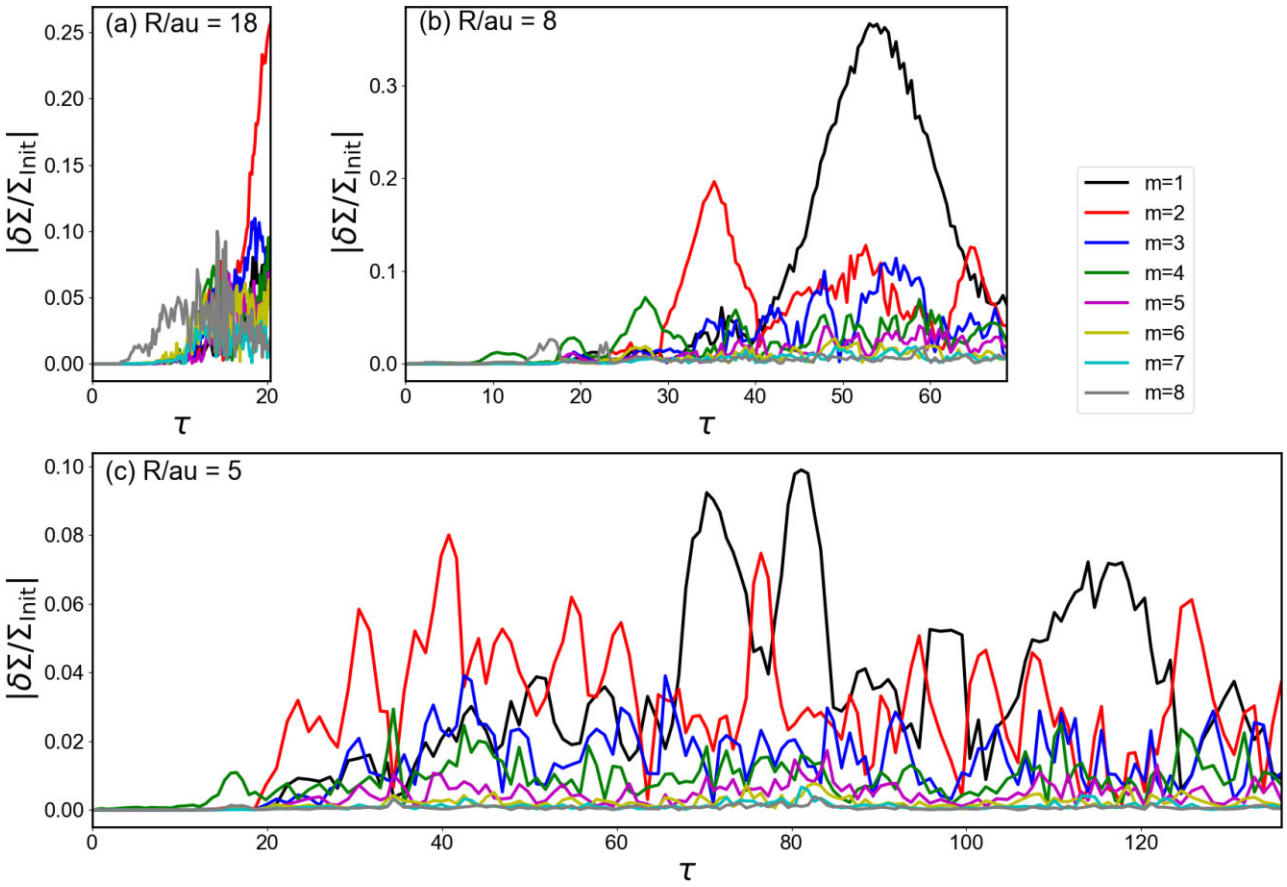

Figure 5. The time evolution of the mode amplitudes of the azimuthal surface density variation for three representative rings at radii of $R \sim 18$ (panel a), 8 (b), and 5 au (c) of Model T-3D-2000. The time is normalized by their local period. Panel (a) shows the $m = 8$ mode first dominates the 18 au ring before being overtaken by the $m = 2$ mode. Panels (b) and (c) illustrate a similar trend: the higher order modes develop first before being overtaken by low-order modes, as expected for RWI modes.

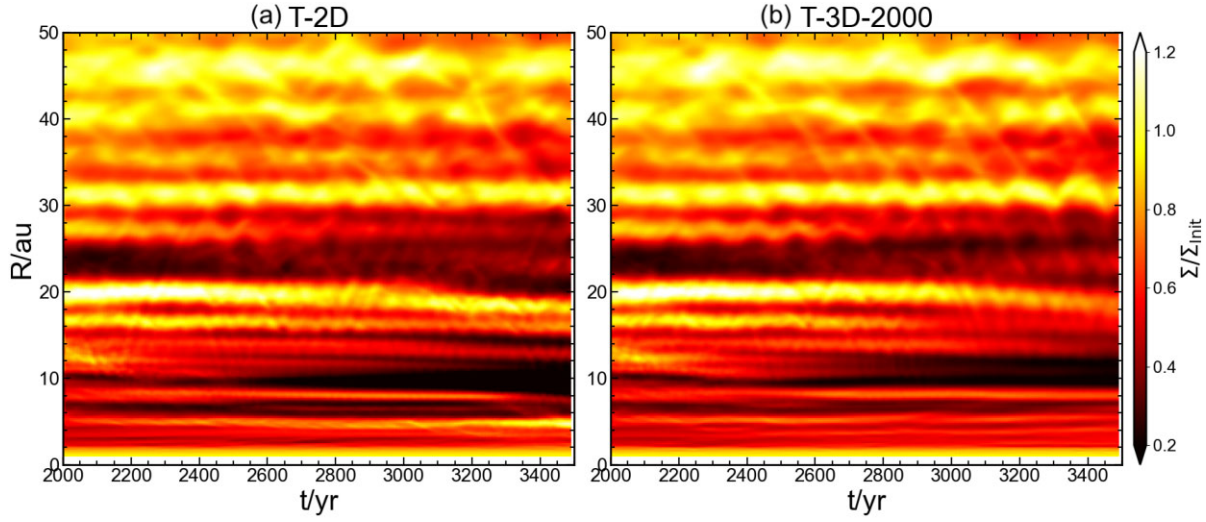

Figure 6. Time evolution of (a) the surface density distribution of Model T-2D and (b) the azimuthally averaged surface density distribution of Model T-3D-2000 as a function of radius after the 3D restart at = 2000 yr. Note the prominent rings and gaps survive in 3D despite RWI.

the $m = 1$ azimuthal mode reaches its peak amplitude (see Fig. 5b). We will concentrate on the broad features of the vortices since their detailed structures may not be adequately resolved in our 3D global non-ideal MHD simulations. At this time, the $m = 2$ mode has a significant amplitude as well, leading to a secondary density peak next to the primary one, as shown in Figs 7(a) and 8(b) (the one with a smaller value of the azimuthal angle ϕ). As expected, these vortices are anticyclonic, with the flow streamlines on the mid-plane circling

Downloaded from https://academic.oup.com/mnras/article/533/3/2980/7737683 by guest on 19 June 2025

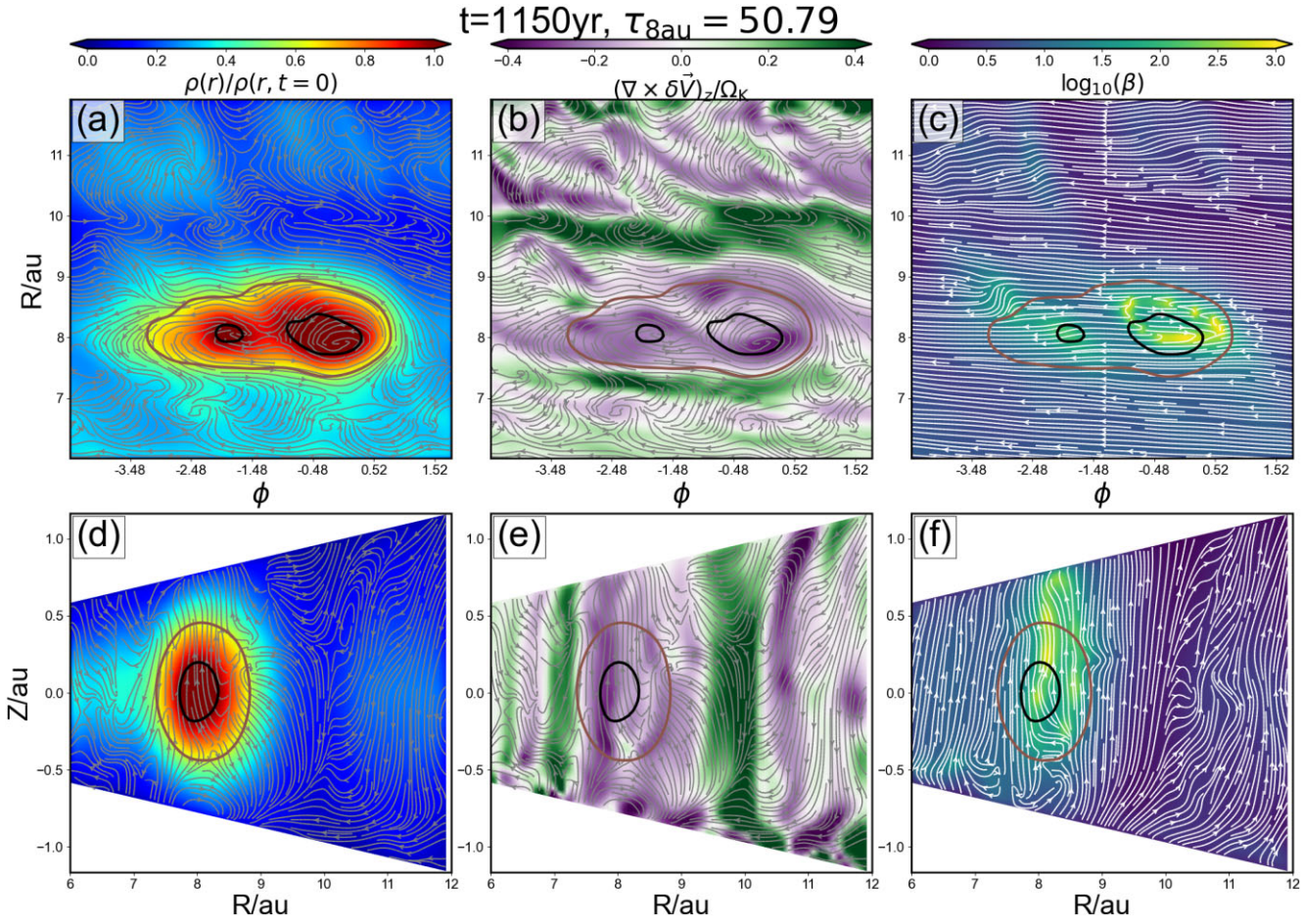

Figure 7. Structure of the dominant vortex in the 8 au ring at $\tau \sim 50$. Panels (a)–(c) show the mass density normalized to its initial value, the $z-$component vorticity normalized to its local Keplerian angular speed, and the logarithmic scale of the plasma-β on the mid-plane, respectively. Panels (a) and (b) include the velocity streamlines (grey lines) and the panel (c) the magnetic fields (white lines). Panels (d) and (f) are the same as (a)–(c), but on a meridional plane passing through the density peak of the 8 au ring. The brown and black contour lines are 0.6 and 1.0 contours of the mass density normalized to its initial value. An animated version of the figure can be found at https://virginia.box.com/s/499xq1qt2j9c9vgxzljlb19x610tfnqe.

the local density maxima in a direction opposite to the Keplerian rotation (see Fig. 7a).

The corresponding negative axial vorticity is shown in panel (b) of Fig. 7. Note that the spatial distributions of the axial vorticity in and around the vortices are patchier compared to 3D hydro simulations (e.g. fig. 8 of Richard et al. 2013), likely because the magnetic fields included in our simulation make the disc more dynamically active and can produce spatially variable vorticity even in the absence of RWI-induced vortices. Nevertheless, regions of high negative vorticity appear relatively coherent in the vertical direction, as shown in their $R - z$ distribution (panel e), similar to the columnar structure seen in the hydro case (e.g. fig. 8 of Richard et al. 2013).

The streamlines in panels (d) and (e) show that the flow on the poloidal $(R - z)$ plane has a downdraft in the outer part of the vortex (with larger radii than that of the density peak) and an updraft in the inner part (near the density peak), with some hint of a clockwise vortex in between. This pattern is reminiscent of the one shown in the lower left panel of fig. 13 of Meheut et al. (2010) (in the region between their ~ 2.8 and 3.0 r_i), who studied the 3D structures of hydro RWI vortices. However, the vortex is barely visible and much less prominent than the hydro case. There is a prominent counterclockwise vortex outside the clockwise one in the hydro case, but not in our case. The difference may not be surprising since our wind-launching non-ideal MHD disc has strong meridional circulation motions, particularly in dense rings (e.g. fig. 8 of Hu et al. 2022; see also Riols & Lesur 2019; Cui & Bai 2021 and Fig. 12d below), which can, in principle, change the dynamics and structure of the RWI vortices.

Specifically, magnetic fields may affect the motions in and around the vortices. For example, the field lines in the $R - \phi$ plane are mostly toroidal (i.e. along ϕ-direction; panel c), which may resist the field bending by the cross-field motion associated with the anticyclonic rotation around the density peak of the vortex (panel a). However, the magnetic fields inside the overdense vortex are relatively weak, corresponding to a typical plasma-β of order 10^2 (panel c), so their direct resistance to the vortex motion may be relatively modest. Nevertheless, the magnetic field and its associated outflow dominate the angular momentum transport and generate strong poloidal motions and non-Keplerian rotation throughout the disc, which could affect the RWI vortices indirectly; indeed, they give rise to the RWI-unstable substructures in the first place. However, such indirect effects are difficult to quantify.

An interesting feature of the plasma-β distribution in the $R - \phi$ plane (panel c) is a ring of high β values offset from the density peak, where the field lines change directions abruptly. Panel (f) shows that the feature extends vertically outside the high-density part of

Downloaded from https://academic.oup.com/mnras/article/533/3/2980/7737683 by guest on 19 June 2025

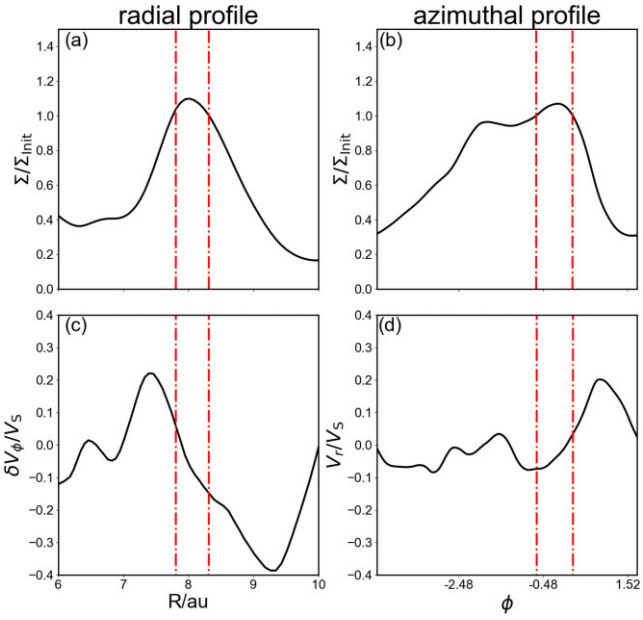

Figure 8. Detailed structure of the dominant RWI vortex in the 8 au ring of the Model T-3D-2000 at $\tau \sim 50$. Panels (a) and (c) show the radial profiles of the surface density normalized to its initial value and azimuthal velocity deviation from the local Keplerian value normalized to local sound speed, respectively, on a meridional plane passing through the density peak at 8 au. Panels (b) and (d) show the azimuthal profiles of the surface density normalized to its initial value and radial velocity normalized to the local sound speed of the same vortex. The red dashed–dotted lines mark the locations where the mass density normalized to its initial value is 1.0 (corresponding to the black density contour in Fig. 7).

the vortex outlined by the isodensity contours, indicating that it is primarily a feature of weak local magnetic field rather than high density. Specifically, it is primarily associated with regions where the magnetic field reversal happens, particularly in the ϕ-direction (i.e. where B_ϕ approaches zero). The field reversal in or near dense vortices is unsurprising because the gas motions there are strong enough to tangle the field lines, creating kinks where the magnetic field components (such as B_ϕ or B_r) drop to zero. Field tangling is harder to achieve in the more strongly magnetized lower density regions (e.g. gaps), where the field lines are straighter.

To analyse the vortices more quantitatively, we plot in Fig. 8 the radial and azimuthal profiles of the normalized surface density across the density peak of the primary vortex (panels a and b) and the radial profile of the deviation of the azimuthal velocity from the local Keplerian value (panel c) and the azimuthal profile of the radial velocity (panel d) normalized by the local sound speed. The radial density profile is asymmetric because the gap outside the vortex-forming ring is deeper than that inside (see Fig. 7 and its animated version). The super-Keplerian rotation radially interior to the density peak and sub-Keplerian rotation exterior to the peak are consistent with expectations. As expected from the counterclockwise circulation pattern of the anticyclonic vortex around the density peak in the $R-\phi$ plane (see Fig. 7a), the radial velocity is positive on the larger azimuthal angle side of the density peak, reaching a maximum of ~ 0.2 times the local sound speed. It is negative on the other side, decreasing to a minimum of only ~ -0.1 times the local sound speed; the asymmetry is caused by the secondary vortex nearby.

An important parameter to characterize a vortex is its aspect ratio $\chi \equiv a/b$, where a and b are the major and minor axes of close

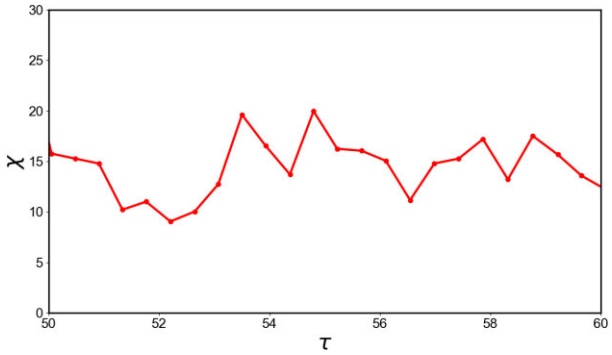

Figure 9. The aspect ratio for the dominant vortex at 8 au in Model T-3D-2000 from $\tau = 50$ to 60 (the time is normalized by the local orbital period).

streamlines (e.g. Ono et al. 2018). Because the velocity field in our non-ideal MHD simulation is much more disordered than the hydro simulations (see the velocity streamline in Fig. 7), we choose to approximate the shape of the vortex using the iso-density contour of $\rho(r,\phi)/\rho(r,t=0) = 1$ (i.e. the black lines for the dominant vortex in Fig. 7a). The resulting aspect ratio χ for the dominant vortex near the 8 au radius is shown in Fig. 9 as a function of time during the period when the $m = 1$ mode dominates ($50 < \tau < 60$; see panel b of Fig. 5). The aspect ratio is of order 10 or larger for the entire duration, indicating that the vortex is highly elongated, consistent with visual inspection of Fig. 7 and especially Fig. 4 and their associated animations. Lesur & Papaloizou (2009) pointed out that vortices in discs tend to be unstable to ellipsoidal instability in 3D, although the maximum growth rate obtained from linear analysis decreases rapidly with increasing aspect ratio χ in a stratified disc (see the red curve in their fig. 6), making it increasingly difficult to detect in simulations. Richard et al. (2013) found that highly elongated vortices with $\chi \sim 6$ or larger can survive in 3D compressible hydro simulations. This hydro result contrasts with our non-ideal MHD simulation, where the amplitude of the dominant $m = 1$ mode at 8 au steadily decreases after peaking around $\tau \approx 55$ despite its large aspect ratio.

There are several possibilities for the above difference. First, the magnetic field in our simulation may weaken the vortex. For example, the circulating flow in the vortex must move across the predominantly toroidal magnetic field in the mid-plane (contrasting the flow streamlines and field lines in, e.g. Figs 7a and c, respectively) and is expected to be resisted by magnetic tension. Lyra & Klahr (2011) found that the elliptic instability is quite destructive in magnetized discs; perhaps this explains why even elongated vortices decay in our simulations. Secondly, the vortex may be weakened by the magnetized disc wind in our simulation. Through mass and angular momentum removal, the wind induces strong meridional circulation that may be incompatible with the columnar structure preferred by the vortex. In particular, significant vertical motions are present in our simulation (see e.g. Fig. 7d), which are different from those found in 3D hydro simulations (e.g. Meheut et al. 2010; Meheut, Yu & Lai 2012; Richard et al. 2013). Thirdly, our wind-launching non-ideal MHD disc is more dynamically active than the relatively quiescent disc envisioned in most of the previous 3D hydro RWI simulations, with an effective α parameter of order 0.01 to 0.1 estimated from the Reynolds and Maxwell stresses, which can negatively impact the vortex's survival (e.g. Lin 2013).

Interestingly, many cyclonic vortices form in our restarted 3D simulation in addition to the anticyclonic vortices discussed above. They are formed in low-density gaps and evolve broadly like the

Downloaded from https://academic.oup.com/mnras/article/533/3/2980/7737683 by guest on 19 June 2025

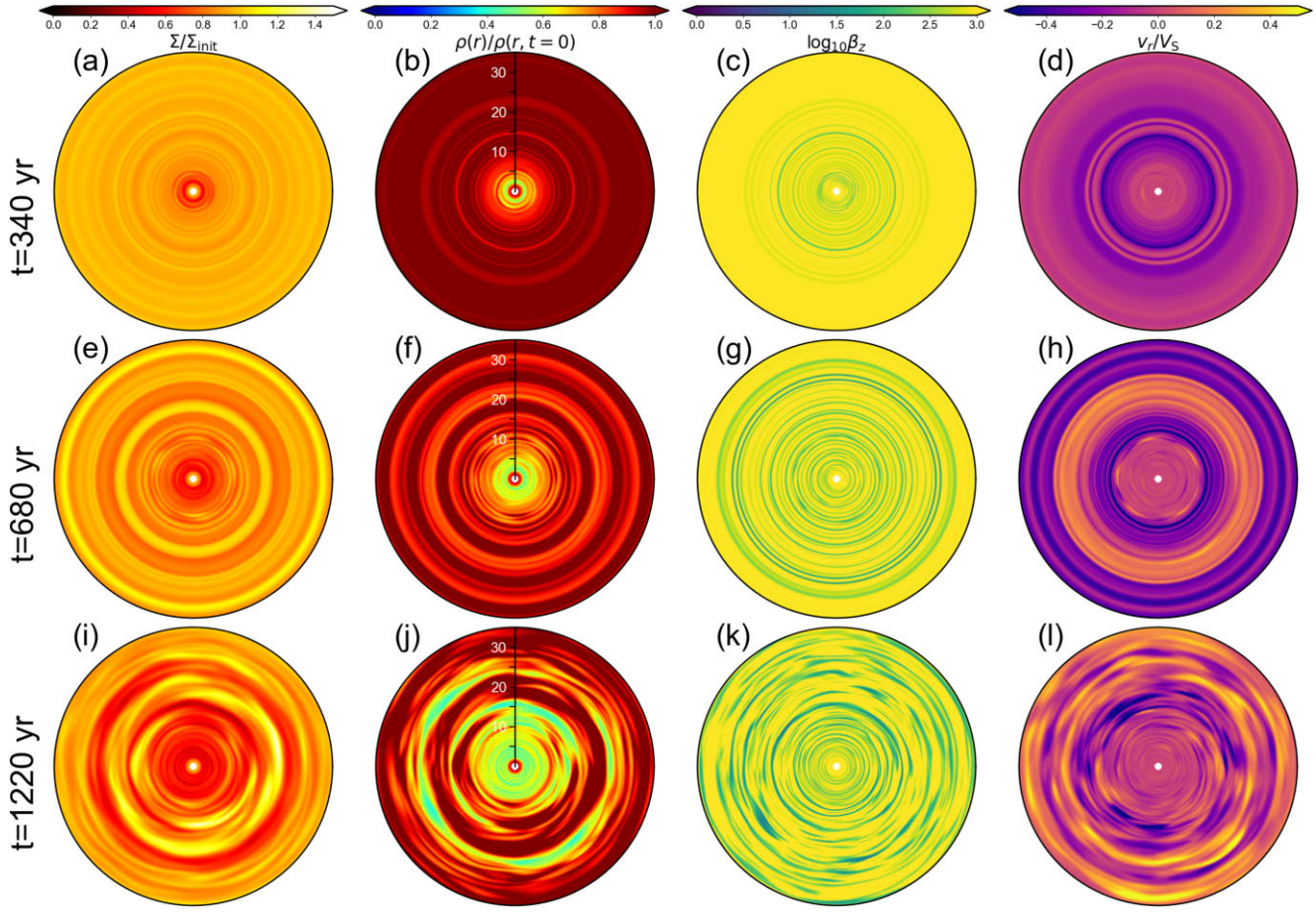

Figure 10. Simultaneous growth of rings and gaps and RWI in 3D in Model T3D-0. Plotted in the first column are the surface density distribution normalized to its initial value at three representative times $t = 340$ (panel a), 680 (panel e), and 1220 yr (panel i). Similarly, the second, third, and fourth columns show, respectively, the mid-plane mass density normalized to its initial value, the mid-plane plasma-β_z based on the vertical field component B_z alone, and the mid-plane radial velocity normalized by the sound speed. An animated version of the figure can be found on the website: https://virginia.box.com/s/shw9ux7dc0klb3bduj13iqvq3hj45rjq.

anticyclonic vortices formed in dense rings: higher order azimuthal modes dominate at earlier times and lower order modes at later times. For example, eight cyclonic vortices (i.e. the $m = 8$ mode) are clearly visible in the ∼10-au gap from the streamlines plotted on the $R - \phi$ plane at a relatively early time $t = 450$ yr after the restart (corresponding to about 14 local orbital periods), as shown in the animated version of Fig. 7. They merge into fewer numbers at later times. In particular, at the time of $t = 1150$ yr shown in Fig. 7, there are only two readily identifiable cyclonic vortices with (clockwise) closed streamlines in the 10-au gap, as can be seen from panel (a) and particularly (b), which also shows that the cyclonic vortices have the largest (positive) vertical component of the vorticity ω_z. Besides the sign of ω_z, these vortices differ from the anticyclonic ones (with a negative ω_z) in one major aspect: they are more strongly magnetized, with a plasma-β typically of order unity, as can be seen from panels (c) and (f). Nevertheless, despite the strong magnetization in the gap, cyclonic vortices appear to be able to develop and survive until the end of the simulation at $t = 1490$ yr after the 3D restart, corresponding to ∼47 local orbital periods at 10 au.

Since the perfectly axisymmetric rings and gaps formed in 2D simulations are shown to be unstable to RWI, such idealized structures are unlikely to be produced in nature without the assumption of axisymmetry. We are thus motivated to start the 3D simulations from the very beginning to determine how the RWI interacts with the formation of the rings and gaps in the first place.

4.4 3D simulation from the beginning

In this section, we analyse the results of Model T-3D-0, which is the same as Model T-3D-2000 but restarts from the 2D simulation at $t = 0$ yr rather than $t = 2000$ yr. Since the disc has no initial substructure, it is initially stable to RWI. We expect the non-axisymmetric RWI modes to grow as rings and gaps develop through non-ideal MHD processes in the wind-launching disc. The initial development of nearly axisymmetric rings and gaps is illustrated in the top panels of Fig. 10, where we plot the normalized column density, the mid-plane density, plasma-β_z based on the vertical component of the magnetic field, and radial velocity normalized by the local sound speed, at the same representative time of $t = 340$ yr as shown in the top panels for Model T-3D-2000 in Fig. 4. In the T-3D-2000 case, a prominent $m = 8$ azimuthal RWI mode has already become clearly visible at this time in a ring around ∼ 11 au radius. In the T-3D-0 case, although rings and gaps have developed near ∼ 10 au at this time, they remain nearly axisymmetric, likely because their amplitudes are still relatively small and it takes time for RWI modes to grow, particularly on a background ring/gap of relatively low contrast.

Downloaded from https://academic.oup.com/mnras/article/533/3/2980/7737683 by guest on 19 June 2025

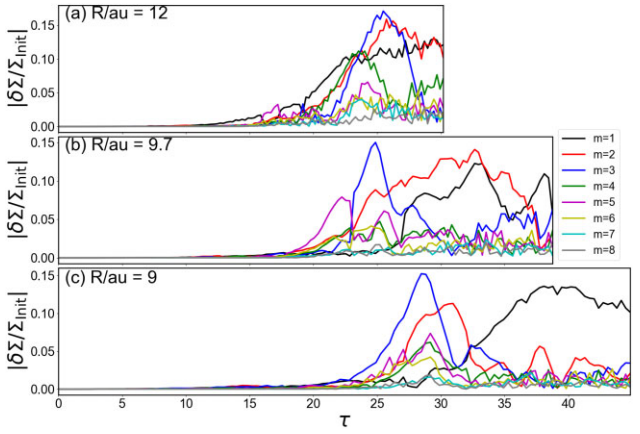

Figure 11. Same as Fig. 5, but for Model T-3D-0 at $R = 12$ (a), 9.7 (b), and 9 au (c).

Non-axisymmetric RWI modes do develop at later times. For example, the middle row of Fig. 10 shows a prominent $m = 5$ mode on a ring of ~ 9.7 au radius at the second representative time of $t = 680$ yr, corresponding to about 22.5 local orbital periods. It is seen most clearly in the radial velocity map (Fig. 10h), but is also visible in the other three maps (Figs 10e–g). At later times, the non-axisymmetric structure becomes more dominated by lower order azimuthal modes (with smaller m), broadly consistent with the trend expected for RWI. For example, at the end of the simulation ($t = 1220$ yr, shown in the bottom row), the azimuthal density perturbation is dominated by a high-density vortex ($m = 1$ mode) near the bottom of the ~ 9.7 au ring, although other low-order ($m = 2$ and $m = 3$) modes are also visible.

To quantify the mode evolution, we plot in Fig. 11 the time evolution of the amplitudes of various azimuthal modes, as done in Fig. 5 for the restarted model T-3D-2000. It is clear that the $m = 5$ mode initially dominates the 9.7 au ring (the purple peak around $\tau \sim 22$). As time progresses, it is first replaced by the $m = 3$ (blue), then $m = 2$ (red), and, finally, $m = 1$ (black) mode. The progression towards lower order modes with time is also evident for the 9 au ring shown (bottom panel), consistent with the expectation of RWI. Interestingly, the top panel shows that the azimuthal modes of the outer 12 au ring are dominated by $m = 1$ at relatively early times between $\tau \sim 13$–16. This is in contrast with the outer (18 au) ring of Model T-3D-2000, which is dominated by the high-order $m = 8$ mode at similarly early times (see the grey curve in the top panel of Fig. 5). We attribute the different behaviour to the difference in the initial disc structure when the 3D simulation starts. In the T-3D-2000 case, highly RWI unstable, well-defined rings of large contrast with their surroundings already exist at the beginning of the simulation (see the red curve in the top panel of Fig. 3). For such (unstable) conditions, the higher order modes are expected to grow faster, as discussed earlier in Section 4.2 (see also, e.g. Ono et al. 2018). In the T-3D-0 case, there is no ring at 12 au (or anywhere else) initially. It takes time for the rings to form out of the initially smooth disc and for their amplitudes to increase relative to their surroundings (see Fig. 13 below). When the ring amplitude is smaller, the fastest growing mode tends to be of a lower order (see e.g. table 1 of Ono et al. 2018), consistent with the above difference between the outer rings of Models T-3D-0 and T3D-2000.

To illustrate the vortices formed in the T-3D-0 model more pictorially, we plot in Fig. 12 the normalized density, vertical component of the vorticity, and the plasma$-\beta$ on the mid-plane and in the meridional plane passing through the centre of a vortex at the same representative time of $t = 680$ yr as in the second row of Fig. 10, similar to the maps shown Fig. 7 for Model T-3D-2000. Compared to the T-3D-2000 case, the density contrast between regions of different radii is much less (compare Figs 12a and 7), which is expected given that the T-3D-2000 model was restarted with already formed high-contrast rings and gaps. Nevertheless, regularly spaced anticyclonic vortices (with negative values of vertical vorticity) are clearly visible at higher density radii (e.g. ~ 9.3 and 10.3 au) and cyclonic vortices (with positive values of vertical vorticity) at lower density radii (e.g. ~ 8.8 and 9.8 au; see panels [a] and [b]), with the cyclonic vortices forming preferentially at azimuthal angles between the anticyclonic ones (and vice versa).

Despite the prominent vortices of both positive and negative vorticities on the $R - \phi$ plane, the flow structure in the meridional plane at this time is rather regular, with a layer of accreting material located approximately near the mid-plane, which drives two prominent cells of opposite meridional circulation above and below the layer near the radius of the dominant anticyclonic vortex marked by the black contour in panel (c). Indeed, associated with the meridional circulations is an azimuthal component of vorticity that is larger than the vertical component, even inside the dominant RWI vortex, as seen by comparing panels (d) and (e) of Fig. 12. The strong meridional circulation, ultimately induced by the magnetic field through accretion and disc wind, is a feature absent from hydro simulations of RWI.

The meridional flow pattern in 3D is nearly identical to that studied in detail in 2D (axisymmetric) simulations (e.g. fig. 8 of Hu et al. 2022). In particular, the accretion layer is associated with regions of vanishing toroidal magnetic fields, where the field lines change directions sharply in the azimuthal direction, creating a large tension force in the (negative) azimuthal direction that brakes the rotation and drives accretion. The weak toroidal field is why the accretion layer shows up as a filament of high plasma$-\beta$ in panel (f). The panel shows clearly that the accretion drags the poloidal field lines into a pinched configuration, which, Suriano et al. (2018) argue, leads to reconnection that lies at the heart of ring and gap formation in the first place. Clearly, the development of RWI in 3D does not shut-off the mechanism for generating rings and gaps in the non-ideal MHD and wind-launching disc in the first place.

The persistence of ring and gap formation despite the RWI is further illustrated in Fig. 13, where we compare the radial distribution of the azimuthally averaged normalized surface density at different times for Model T-3D-0 and its 2D counterpart T2D. As in the T-3D-2000 case (see Fig. 6), the contrast between the rings and gaps tends to be somewhat less in 3D than in 2D. Nevertheless, rings and gaps have clearly developed and persisted until the end of the simulation. It can also be seen from the animated version of Fig. 10 (see its caption for a link to the animation).

We believe the ring and gap formation persists because the RWI modifies but does not fundamentally change the flow structures that enable the formation and growth of rings and gaps. This is illustrated in Fig. 14. The top left panel shows a much lower plasma-β_θ (based on the θ-component of the magnetic field) in the low-density gaps than in the dense rings, consistent with the result from earlier work that the poloidal magnetic flux tends to be redistributed from the rings to the gaps. This poloidal magnetic flux redistribution pattern is fundamental to the MHD mechanism of ring and gap formation (e.g. Suriano et al. 2018; Riols & Lesur 2019; Cui & Bai 2021). It is broadly preserved in 3D, as seen in the three lower left panels, which plot the meridional distributions of the plasma-β_θ at three representative azimuthal angles. Also evident from the panels

Downloaded from https://academic.oup.com/mnras/article/533/3/2980/7737683 by guest on 19 June 2025

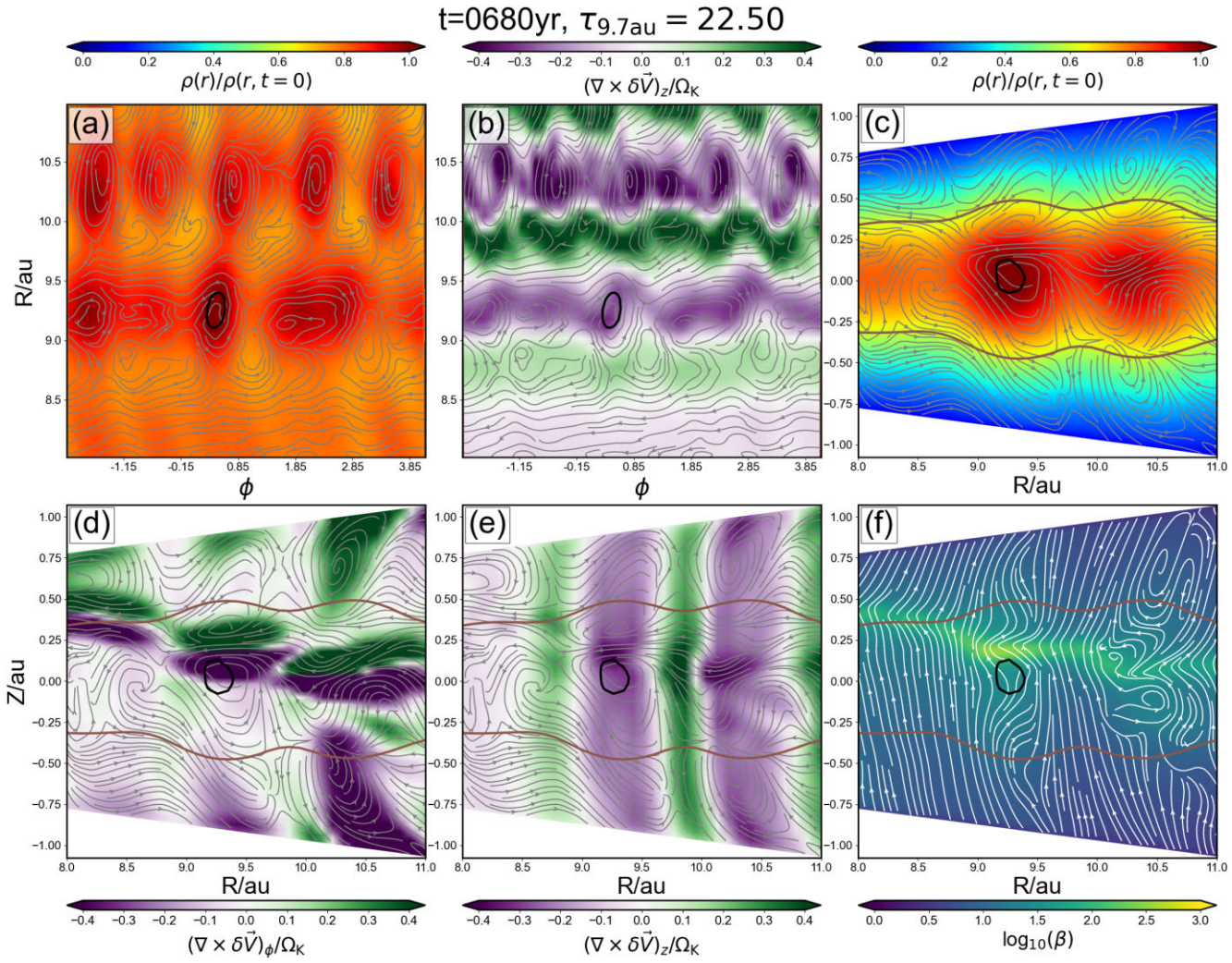

Figure 12. The structure of the dominant vortex on the 9.7 au ring in Model T-3D-0 at $\tau \sim 22.5$. Panels (a) and (b) display the mass density normalized to its initial value at the mid-plane and the z-component vorticity normalized to its local Keplerian period, respectively. Panels (c)–(f) plot the mass density normalized to its initial value (c), the ϕ-component of the vorticity normalized to its local Keplerian period (d), the z-component vorticity normalized to its local Keplerian period (e), and the logarithm of the plasma-β (f) on a meridional plane passing through the density peak of the ~ 9.2 au ring. The grey contours with arrows are velocity streamlines and the white contours (in panel [f]) with arrows are the magnetic field lines. The brown and black contour lines mark where the mass density normalized to its initial value is 0.6 and 1.0, respectively. An animated version of the figure can be found at https://virginia.box.com/s/oofe09pt2qv01wkk42vv8e0tzqg3oy7k.

are azimuthal variations of the density (particularly in the rings between ~ 10 and 15 au) and the plasma-β_θ (particularly around ~ 16 au where its value is much higher at $\phi = 4\pi/3$ than at $\phi = 0$ and $2\pi/3$). Similarly, the characteristic disc flow structure in 2D, with the accretion concentrating in warped layers (especially within about 20 au radius where most rings and gaps are located; see the blue regions in the top right panel), is broadly preserved in 3D. Suriano et al. (2018) argued that this flow structure is important for ring and gap formation because it generates sharp pinching of the poloidal magnetic field, facilitating reconnection and magnetic flux redistribution relative to mass. There are azimuthal variations in the accretion flow, as seen in the three lower right panels around, for example, the ∼15-au radius. They appear to modify but not destroy the rings and gaps.

A caveat of our simulations is that, despite the use of SMR, the resolution may not be high enough to fully resolve any MRI turbulence that may develop, especially in the relatively well (magnetically) coupled outer part of the disc beyond ~ 40 au, where the initial ambipolar Elsasser number on the mid-plane exceeds 10 for the 3D models discussed in this section (see the red curve in the upper panel of Fig. A2). Although our focus is on the less well-coupled inner disc (inside ~ 30 au) that is expected to be less prone to MRI than the outer disc, it is possible that its dynamics and structure can be modified at a higher resolution, where a better resolved MRI turbulence can potentially reduce the amplitudes of the rings and gaps and increase their widths, making them more stable to RWI. Indeed, there are no obvious vortices in the 3D model shown in fig. 10 of Cui and Bai (2021), which has a higher resolution than ours but a smaller azimuthal angle range ($\pi/4$ rather than 2π). Whether the limited azimuthal angle range has a strong effect on the formation and evolution of RWI vortices or not remains to be determined. Higher resolution simulations with a full azimuthal angle range are desirable to resolve the potential discrepancy.

Downloaded from https://academic.oup.com/mnras/article/533/3/2980/7737683 by guest on 19 June 2025

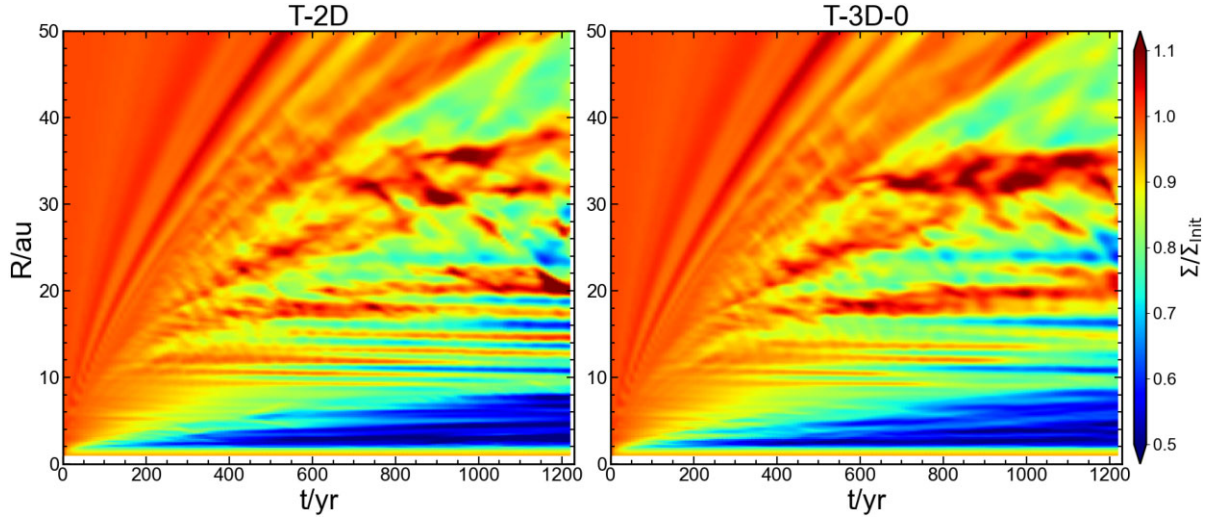

Figure 13. Same as the Fig. 6, but for the Model T-3D-0 and with a different colour bar.

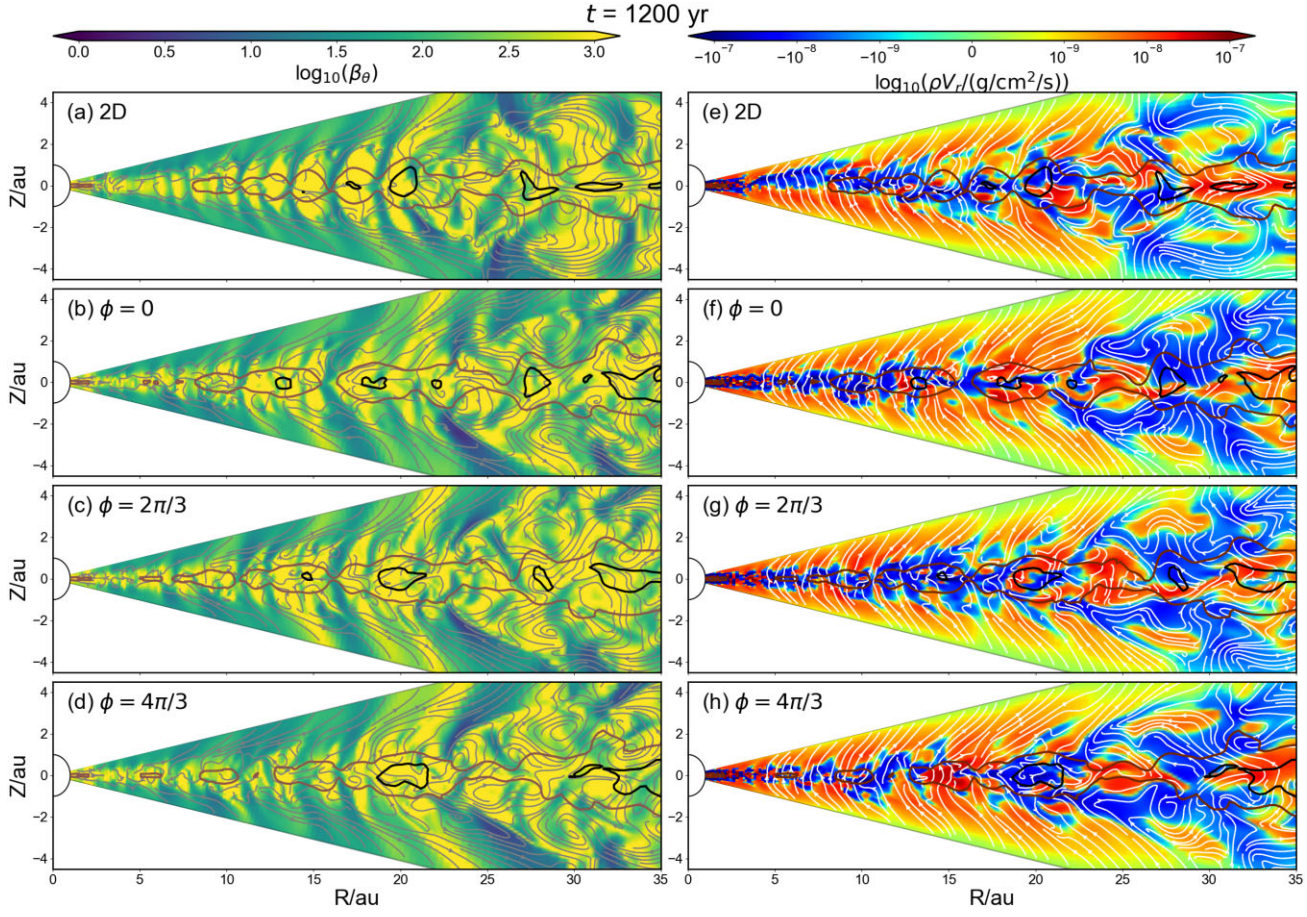

Figure 14. Comparison of the 2D and 3D meridional structures at a representative time $t = 1200$ yr. The left panels plot the logarithmic scale of plasma β_θ (based on the polar component of the magnetic field), with velocity streamlines traced by the grey lines with arrows. The right panels plot the radial mass flux per unit area, with the magnetic field lines traced by the white lines with arrows. The top panels are for the axisymmetric model T-2D, and the lower three panels are for three meridional planes of the 3D Model T-3D-0 with, respectively, $\phi = 0$, $2\pi/3$, and$4\pi/3$. The brown and black contour lines mark where the mass density normalized to its initial value is 0.6 and 1.0, respectively.

Downloaded from https://academic.oup.com/mnras/article/533/3/2980/7737683 by guest on 19 June 2025

5 CONCLUSION

We performed 2D (axisymmetric) and fully 3D non-ideal MHD simulations of substructure formation in magnetized, weakly ionized, wind-launching discs, with the non-ideal MHD coefficients computed from a simplified chemical network including dust grains. A 2D simulation using a simple power-law prescription for the ionization fraction is also included for comparison. We focused on whether the substructures formed in such discs are stable to the RWI and, if not, how the RWI affects the formation and evolution of the substructures. Our main conclusions are summarized as follows.

(i) In agreement with previous work, axisymmetric gas rings and gaps form spontaneously in 2D simulations of non-ideal MHD discs with ambipolar diffusion and Ohmic dissipation, with more prominent substructures for larger Elsasser numbers (or better magnetic coupling). The case for non-ideal MHD formation of substructures is thus strengthened, at least under the assumption of axisymmetry.

(ii) Axisymmetric gas rings in 2D simulations are found to be unstable to RWI according to analytic stability conditions and through 3D restart simulation. As expected for RWI, shorter wavelength (or larger m) azimuthal modes develop earlier in the simulation, and longer wavelength ones dominate later, forming elongated anticyclonic vortices (arcs) in the ring's column density distribution that last until the end of the simulation. Highly elongated vortices with aspect ratios of 10 or more are found to decay with time in our simulation, in contrast with the hydro case. This difference could be caused by magnetically induced motions, particularly strong meridional circulations with large values of azimuthal vorticity, which may be incompatible with the columnar structure preferred by vortices. Axisymmetric gaps in the 2D simulation are also unstable to RWI, forming cyclonic vortices despite being strongly magnetized, with a plasma-β of order unity. Nevertheless, the cyclonic and anticyclonic RWI vortices modify but do not destroy the rings and gaps in the radial gas distribution of the disc.

(iii) Our 3D simulation that starts from a smooth initial condition shows that RWI does not shut-off the mechanism for generating rings and gaps in the non-ideal MHD and wind-launching disc. Specifically, anticyclonic and cyclonic vortices are still formed in rings and gaps, respectively, with amplitudes saturating at moderate levels. The RWI and associated vortices modify but do not suppress the poloidal magnetic flux accumulation in low-density regions and the characteristic meridional flow patterns that are crucial to the ring and gap formation.

An interesting question to address in future investigations is how RWI affects the dust distribution and the disc appearance in continuum emission. Most observed disc dust substructures appear rather axisymmetric, although a small fraction shows non-axisymmetric features, including arcs, which are potentially vortices. The RWI vortices discussed in this paper open up the possibility of producing such dusty vortices in non-ideal MHD wind-launching discs. However, detailed dust treatment is needed to explore this possibility quantitatively. The current simulation will also benefit from adaptive (rather than static) mesh refinement, which will better resolve the vortices formed in the global 3D simulations. Higher resolution is also desirable to better resolve any MRI turbulence that may develop, which can modify the disc dynamics and structure, which, in turn, affects its stability to RWI.

ACKNOWLEDGEMENTS

We thank the referee, Dr Cui, Can, for a prompt and constructive report. CYH acknowledges support from NASA SOFIA grant SOF-10_0505 and NRAO ALMA Student Observing Support (SOS) and computing resources from UVA research computing (RIVANNA) and NASA High-Performance Computing. ZYL is supported in part by NASA 80NSSC20K0533 and NSF AST-2307199. MKL is supported by the National Science and Technology Council (grants 111-2112-M-001-062-, 112-2112-M-001-064-, 111-2124-M-002-013-, and 112-2124-M-002-003-) and an Academia Sinica Career Development Award (AS-CDA110-M06).

DATA AVAILABILITY

The data underlying this article will be shared on reasonable request to the corresponding author.

REFERENCES

ALMA Partnership et al., 2015, ApJ, 808, L3
Andrews S. M. et al., 2018, ApJ, 869, L41
Bae J., Zhu Z., Hartmann L., 2017, ApJ, 850, 201
Bae J., Isella A., Zhu Z., Martin R., Okuzumi S., Suriano S., 2023, in Inutsuka S., Aikawa Y., Muto T., Tomida K., Tamura M.eds, ASP Conf. Ser. Vol. 534, Protostars and Planets VII. Astron. Soc. Pac., San Francisco, p. 423
Bai X.-N., Stone J. M., 2013, ApJ, 769, 76
Bai X.-N., Stone J. M., 2017, ApJ, 836, 46
Boehler Y. et al., 2021, A&A, 650, A59
Cimerman N. P., Rafikov R. R., 2023, MNRAS, 519, 208
Cui C., Bai X.-N., 2021, MNRAS, 507, 1106
Cui C., Tripathi A., Yu C., Lin M.-K., Youdin A., 2024, preprint (arXiv:2407.02103)
Dong R., Zhu Z., Whitney B., 2015, ApJ, 809, 93
Draine B. T., Sutin B., 1987, ApJ, 320, 803
Flock M., Ruge J. P., Dzyurkevich N., Henning T., Klahr H., Wolf S., 2015, A&A, 574, A68
Galametz M. et al., 2018, A&A, 616, A139
Grassi T., Padovani M., Ramsey J. P., Galli D., Vaytet N., Ercolano B., Haugbølle T., 2019, MNRAS, 484, 161
Hu X., Li Z.-Y., Zhu Z., Yang C.-C., 2022, MNRAS, 516, 2006
Johansen A., Youdin A., Klahr H., 2009, ApJ, 697, 1269
Krapp L., Gressel O., Benítez-Llambay P., Downes T. P., Mohandas G., Pessah M. E., 2018, ApJ, 865, 105
Le Gouellec V. J. M. et al., 2020, A&A, 644, A11
Lesur G. R. J., 2021, A&A, 650, A35
Lesur G., Papaloizou J. C. B., 2009, A&A, 498, 1
Lesur G. et al., 2022, preprint (arXiv:2203.09821)
Li H., Finn J. M., Lovelace R. V. E., Colgate S. A., 2000, ApJ, 533, 1023
Li H., Colgate S. A., Wendroff B., Liska R., 2001, ApJ, 551, 874
Lin M.-K., 2012, ApJ, 754, 21
Lin M.-K., 2013, ApJ, 765, 84
Liu B., Goree J., Nosenko V., Boufendi L., 2003, Phys. Plasmas, 10, 9
Lovelace R. V. E., Li H., Colgate S. A., Nelson A. F., 1999, ApJ, 513, 805
Lyra W., Klahr H., 2011, A&A, 527, A138
Lyra W., Mac Low M.-M., 2012, ApJ, 756, 62
Lyra W., Johansen A., Klahr H., Piskunov N., 2008, A&A, 491, L41
Marr M., Dong R., 2022, ApJ, 930, 80
Mathis J. S., Rumpl W., Nordsieck K. H., 1977, ApJ, 217, 425
Maury A. J. et al., 2018, MNRAS, 477, 2760
McElroy D., Walsh C., Markwick A. J., Cordiner M. A., Smith K., Millar T. J., 2013, A&A, 550, A36
Meheut H., Casse F., Varniere P., Tagger M., 2010, A&A, 516, A31
Meheut H., Yu C., Lai D., 2012, MNRAS, 422, 2399
Nishi R., Nakano T., Umebayashi T., 1991, ApJ, 368, 181
Nolan C. A., Zhao B., Caselli P., Li Z. Y., 2023, MNRAS, 525, 5450

Downloaded from https://academic.oup.com/mnras/article/533/3/2980/7737683 by guest on 19 June 2025

Okuzumi S., Momose M., Sirono S.-i., Kobayashi H., Tanaka H., 2016, ApJ, 821, 82
Ono T., Muto T., Takeuchi T., Nomura H., 2016, ApJ, 823, 84
Ono T., Muto T., Tomida K., Zhu Z., 2018, ApJ, 864, 70
Pinto C., Galli D., Bacciotti F., 2008, A&A, 484, 1
Richard S., Barge P., Le Dizès S., 2013, A&A, 559, A30
Riols A., Lesur G., 2019, A&A, 625, A108
Ruge J. P., Flock M., Wolf S., Dzyurkevich N., Fromang S., Henning T., Klahr H., Meheut H., 2016, A&A, 590, A17
Shu F. H., 1992, Physics of Astrophysics, Vol. II. University Science Books, Mill Valley, CA
Stone J. M., Tomida K., White C. J., Felker K. G., 2020, ApJS, 249, 4
Suriano S. S., Li Z.-Y., Krasnopolsky R., Shang H., 2017, MNRAS, 468, 3850
Suriano S. S., Li Z.-Y., Krasnopolsky R., Shang H., 2018, MNRAS, 477, 1239
Takahashi S. Z., Inutsuka S.-i., 2016, AJ, 152, 184
Tominaga R. T., Takahashi S. Z., Inutsuka S.-i., 2020, ApJ, 900, 182
Umebayashi T., Nakano T., 1990, MNRAS, 243, 103
Umurhan O. M., 2010, A&A, 521, A25
Varnière P., Tagger M., 2006, A&A, 446, L13
Wardle M., 2007, Ap&SS, 311, 35
Yu C., Lai D., 2013, MNRAS, 429, 2748
Yu C., Li H., 2009, ApJ, 702, 75
Zanni C., Ferrari A., Rosner R., Bodo G., Massaglia S., 2007, A&A, 469, 811
Zaqarashvili T. V. et al., 2021, Space Sci. Rev., 217, 15
Zhao B., Caselli P., Li Z.-Y., 2018, MNRAS, 478, 2723

SUPPORTING INFORMATION

Supplementary data are available at *MNRAS* online.

T-3D-2000-vortices_8au.mp4
T-3D-0-vortices_97au.mp4
T-3D-2000-movie_parameters.mp4
T-3D-0-movie_parameters.mp4

Please note: Oxford University Press is not responsible for the content or functionality of any supporting materials supplied by the authors. Any queries (other than missing material) should be directed to the corresponding author for the article.

APPENDIX A: CHARGE ABUNDANCES AND ELSASSER NUMBERS

One of our improvements over previous work along a similar line (Suriano et al. 2018; Hu et al. 2022) is that we computed the charge abundances from a reduced chemical network (see Section 3) rather than using the simple power-law prescription of Shu (1992), which is derived under the assumption of one dominant molecular ion (e.g. HCO^+) and no dust grains. Fig. A1 shows fractional abundances of the main charges computed from our chemical network as a function of number density for an MRN-like dust size distribution with $a_{\rm min} = 0.5\mu$m and $a_{\rm max} = 25\mu$m, including Mg^+, m^+ (molecular ions other than H_3^+), grains with charge 0, $\pm e$, and $\pm 2e$. The power-law prescription of Shu (1992) is also shown for comparison.

We use the charge abundances in Fig. A1 to calculate the Elsasser number together with the disc properties. Fig. A2 shows the initial profile of the ambipolar Elsasser numbers of Model S-2D (where

Table A1. Relative abundances of the elements included in the chemical network. Similar to table 1 of Umebayashi & Nakano (1990), with the fractions remaining in the gas phase set to $\delta_1 = 0.2$ and $\delta_2 = 0.02$.

Element	Abundant	Chemical species	Fraction (gas)
H	1	H_2	1
He	8.5×10^{-2}	He	1
C	4.2×10^{-4}	CO	δ_1
O	6.9×10^{-4}		
	9.0×10^{-5}	O	δ_1
	9.0×10^{-5}	O_2	δ_1
Mg	1.7×10^{-4}	Mg	δ_2

Table A2. List of gas-phase reactions in our chemical network. Symbols α_c, β_c, and γ_c are the coefficients used to determine the reaction rates. These coefficients are grabbed from UMIST database.

Reaction	α_c	β_c	γ_c
$H^+ + O \longrightarrow O^+ + H$	6.86×10^{-10}	0.26	224.30
$H^+ + O_2 \longrightarrow O_2^+ + H$	2.00×10^{-9}	0.0	0.0
$H^+ + Mg \longrightarrow Mg^+ + H$	1.1×10^{-9}	0.0	0.0
$He^+ + H_2 \longrightarrow H^+ + H + He$	7.2×10^{-15}	0.0	0.0
$He^+ + CO \longrightarrow C^+ + O + He$	1.6×10^{-9}	0.0	0.0
$He^+ + O_2 \longrightarrow O^+ + O + He$	1.1×10^{-9}	0.0	0.0
$H_3^+ + CO \longrightarrow HCO^+ + H_2$	1.36×10^{-9}	−0.14	−3.40
$H_3^+ + O \longrightarrow OH^+ + H_2$	7.98×10^{-10}	−0.16	1.4
$H_3^+ + O_2 \longrightarrow O_2H^+ + H_2$	9.3×10^{-10}	0.0	100.0
$H_3^+ + Mg \longrightarrow Mg^+ + H_2 + H$	1.0×10^{-9}	0.0	0.0
$C^+ + H_2 \longrightarrow CH_2^+ + h\nu$	2.0×10^{-16}	−1.3	23.0
$C^+ + O_2 \longrightarrow CO^+ + O$	3.42×10^{-10}	0.0	0.0
$C^+ + O_2 \longrightarrow O^+ + CO$	4.54×10^{-10}	0.0	0.0
$C^+ + Mg \longrightarrow Mg^+ + C$	1.1×10^{-9}	0.0	0.0
$O_2^+ + Mg \longrightarrow Mg^+ + O_2$	1.2×10^{-9}	0.0	0.0
$HCO^+ + Mg \longrightarrow Mg^+ + HCO$	2.9×10^{-9}	0.0	0.0
$H^+ + e \longrightarrow H + h\nu$	3.5×10^{-12}	−0.75	0.0
$He^+ + e \longrightarrow He + h\nu$	5.36×10^{-12}	−0.50	0.0
$H_3^+ + e \longrightarrow H + H + H$	4.36×10^{-8}	−0.52	0.0
$H_3^+ + e \longrightarrow H_2 + H$	2.34×10^{-8}	−0.52	0.0
$C^+ + e \longrightarrow C + h\nu$	2.36×10^{-12}	−0.29	−17.6
$Mg^+ + e \longrightarrow Mg + h\nu$	2.78×10^{-12}	−0.68	0.0
$CO^+ + e \longrightarrow O + C$	2.0×10^{-7}	−0.48	0.0
$O_2^+ + e \longrightarrow O + O$	1.95×10^{-7}	−0.70	0.0
$OH^+ + e \longrightarrow O + H$	3.75×10^{-8}	−0.50	0.0
$O_2H^+ + e \longrightarrow O_2 + H$	3.0×10^{-7}	−0.50	0.0
$HCO^+ + e \longrightarrow CO + H$	2.4×10^{-7}	−0.69	0.0
$CH_2^+ + e \longrightarrow C + H_2$	7.68×10^{-8}	−0.60	0.0

Downloaded from https://academic.oup.com/mnras/article/533/3/2980/7737683 by guest on 19 June 2025

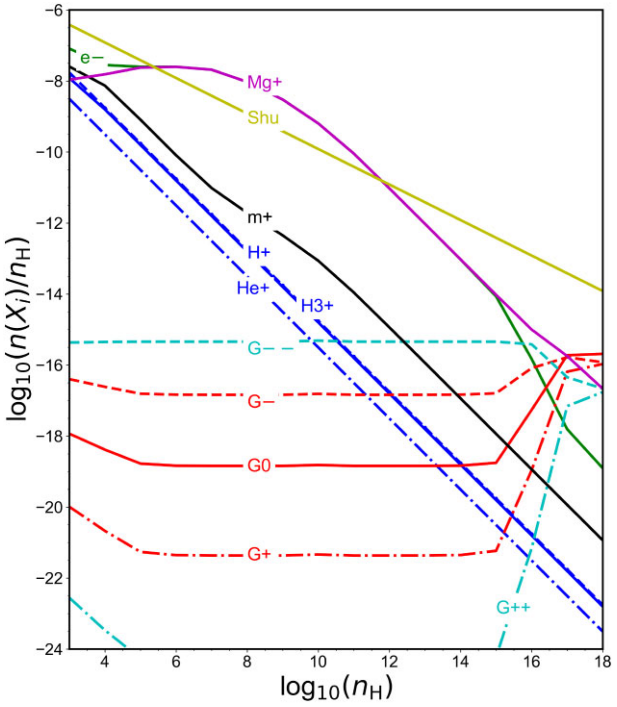

Figure A1. Fractional abundances of main charges as a function of the number density computed from the chemical network for an MRN-type dust size distribution with $a_{\rm min} = 0.5\mu$m and $a_{\rm max} = 25\mu$m. Magnesium ions, molecular ions other than H_3^+, grains with charge 0, $\pm e$, and $\pm 2e$. The power-law prescription of Shu (1992) is plotted as a yellow line for comparison.

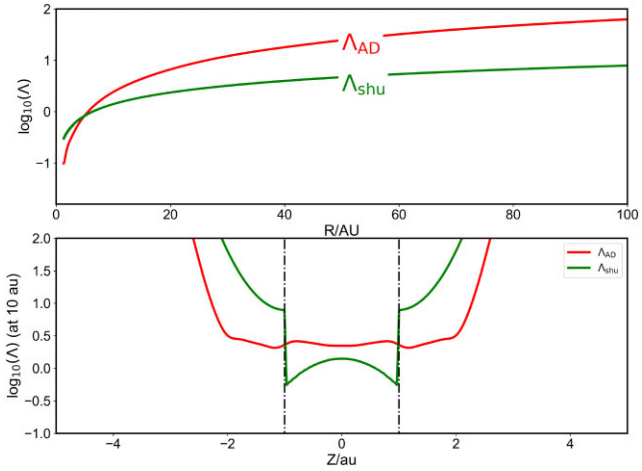

Figure A2. Initial profiles of the ambipolar Elsasser number for Model S-2D (green lines) and Model T-2D (red lines). Panel (a) shows the Elsasser numbers as a function of radius on the mid-plane. Panel (b) shows the Elsasser number at the radius $r = 10$ au as a function of the vertical distance from the mid-plane. The dashed lines in panel (b) mark the disc surface near ~ 1 au.

the power-law prescription of Shu 1992 is adopted; green lines) and Model T-2D (where the chemical network is used; red lines) as a function of radius on the mid-plane (panel a) and as a function of vertical distance from the midplane at $r = 10$ au (panel b, where the θ-dependence in equation [25] is applied).

APPENDIX B: RATE COEFFICIENTS FOR COLLISIONAL MOMENTUM TRANSFER

Three charged species (ions, electrons, and grains) collide with the molecular hydrogen in our model. We take the collisional momentum transfer rate coefficients from Pinto et al. (2008) and Grassi et al. (2019). Note that the units of $R_{e,n}$, $R_{i,n}$, and $R_{g,n}$ in this subsection are $\mathrm{cm^3 s^{-1}}$, corresponding to the $R_{j,n}(T)$ in the equation (21), so the Hall parameter is dimensionless.

For the collisional rate between electrons and molecular hydrogen, we use the rate

$$R_{e,n}(T)=10^{-9}\sqrt{T}\left[0.535+0.203\log_{10}(\mathrm{T})-0.163[\log_{10}(\mathrm{T})]^2\right]. \quad \text{(B1)}$$

The collisional rate between ions and molecular hydrogen is given as

$$R_{i,n}(T) = 2.21\pi\sqrt{\frac{\alpha_{\rm pol}e^2}{m_{\rm red}}}, \quad \text{(B2)}$$

where $\alpha_{\rm pol} = 8.06 \times 10^{-25}\mathrm{cm^3}$ is the polarizability of molecular hydrogen.

The momentum transfer through collisions between charged grains and neutral hydrogen is

$$\langle R_{g,n}(T,Z)\rangle = 2.21\pi\sqrt{\frac{\alpha_{\rm pol}|Z|e^2}{m_{\rm red}}}\frac{a_{\rm c}^{p+1}-a_{\rm min}^{p+1}}{a_{\rm max}^{p+1}-a_{\rm min}^{p+1}} + \left(\frac{8k_{\rm B}T}{\pi m_{\rm r}}\right)^{1/2}\frac{4\pi\delta_{\rm L}}{3}\frac{a_{\rm max}^{p+3}-a_{\rm c}^{p+3}}{a_{\rm max}^{p+1}-a_{\rm min}^{p+1}}\frac{p+1}{p+3}, \quad \text{(B3)}$$

where

$$a_c(T,Z) = \frac{0.206}{\sqrt{\delta_{\rm L}}}\left(\frac{\alpha_{\rm pol}|Z|}{T}\right)^{1/4} \quad \text{(B4)}$$

is a critical grain size to measure microscope grain-neutral reaction for the hard sphere and the Langevin rates (Pinto et al. 2008). We set $\delta_{\rm L} = 1.3$ as recommended by Liu et al. (2003).

This paper has been typeset from a TEX/LATEX file prepared by the author.

Downloaded from https://academic.oup.com/mnras/article/533/3/2980/7737683 by guest on 19 June 2025

© 2024 The Author(s).
Published by Oxford University Press on behalf of Royal Astronomical Society. This is an Open Access article distributed under the terms of the Creative Commons Attribution License (https://creativecommons.org/licenses/by/4.0/), which permits unrestricted reuse, distribution, and reproduction in any medium, provided the original work is properly cited.